eTransportation 28 (2026) 100567

Contents lists available at ScienceDirect

eTransportation

journal homepage: www.journals.elsevier.com/etransportation

Daily operational impacts on battery degradation in heavy-duty electric drayage trucks☆

Ankur Shiledar [a,b,1,*], Joseph N.E. Lucero [c,d,1,*], Ruixiao Sun [e], Manfredi Villani [a,b], Vivek A. Sujan [e], Simona Onori [c,f], Giorgio Rizzoni [a,b]

[a] Department of Mechanical and Aerospace Engineering, The Ohio State University, 201 W 19th Ave, Columbus, 43210, OH, USA
[b] Center for Automotive Research, The Ohio State University, 930 Kinnear Rd., Columbus, 43212, OH, USA
[c] Applied Energy Division, SLAC National Accelerator Laboratory, Menlo Park, 94025, CA, USA
[d] Department of Chemistry, Stanford University, Stanford, 94305, CA, USA
[e] Building and Transportation Science Division, Oak Ridge National Laboratory, Knoxville, 37932, TN, USA
[f] Department of Energy Science and Engineering, Stanford University, Stanford, 94305, CA, USA

ARTICLE INFO

Keywords:
Heavy-duty commercial vehicles
Electrification
Li-ion batteries
Battery degradation

ABSTRACT

Battery aging is a critical factor influencing the performance, longevity, and cost of ownership of battery electric trucks (BETs). This paper presents a comprehensive evaluation of battery aging for two Li-ion battery chemistries, Nickel-Manganese-Cobalt (NMC) and Lithium-Iron-Phosphate (LFP), accounting for both cycling and calendar aging. In contrast to traditional methods that rely on simplified linear degradation models based on manufacturer-provided data, this study employs semi-empirical aging models calibrated to experimentally collected data. The models are integrated into a detailed vehicle simulation environment, enabling a comprehensive assessment of battery degradation under realistic operating conditions. A case study focusing on heavy-duty electric drayage truck operations in the Port of Savannah, GA, is presented to illustrate the impact on battery pack lifespan of: seasonal variations, daily operational activities, charging strategies, and battery storage conditions. The results illuminate the significance of the battery pack's state of charge during stationary periods, such as overnight storage or weekend parking, on battery degradation and its potential implications for long-term vehicle viability. Additionally, the study explores how different operational and environmental factors affect battery degradation, offering critical insights into best battery charging and storage practices. Our results demonstrate that LFP outperforms NMC in terms of years of useful life; however, by utilizing charging strategies that minimize the amount of time the battery spends resting at high levels of state-of-charge, the lifespan of the battery pack that uses NMC can nonetheless be increased by more than a factor of two.

1. Introduction

The transition to battery electric vehicles (BEVs) has gained significant attention as a pathway to improve the energy efficiency of the transportation sector. Heavy-duty commercial vehicles (HDCVs), characterized by high energy demand and long daily utilization, are prime candidates for electrification due to the opportunity for improved operational efficiency, reduced fuel cost volatility, and enhanced energy supply resilience [1,2]. Previous studies such as Fleming et al. [3] and Forrest et al. [4] highlight the technical feasibility and environmental benefits of electrifying medium- and heavy-duty vehicles, citing substantial reductions in harmful air pollutants; however, electrification of this segment faces challenges stemming from high energy requirements, the need to cover long driving distances, and the absence of a robust charging infrastructure [5].

* Corresponding authors.
E-mail addresses: shiledar.1@osu.edu (A. Shiledar), jlucero@stanford.edu (J.N.E. Lucero).

[1] These authors contributed equally.

https://doi.org/10.1016/j.etran.2026.100567
Received 13 April 2025; Received in revised form 8 February 2026; Accepted 15 February 2026
Available online 18 February 2026

At the core of HDCV electrification is the performance and longevity of Lithium-ion batteries (LIBs), which dominate the current BEV market. LIBs are preferred for their relatively high energy density, long cycle life, and favorable performance under diverse environmental conditions. Among LIB chemistries, Nickel-Manganese-Cobalt (NMC) and Lithium-Iron-Phosphate (LFP) are widely used in EVs, each offering distinct advantages [6]. NMC batteries deliver higher energy density, making them suitable for applications requiring longer ranges. Conversely, LFP batteries exhibit greater thermal stability and longer cycle life, making them more durable under the high-current demands typical of HDCVs [7,8]. Despite these advantages, LIBs are prone to long-term degradation including capacity and power fade, which directly impact vehicle performance and operational costs [9].

Understanding the mechanisms of battery degradation is essential to improving the reliability of BEVs in heavy-duty applications. Battery aging can be categorized into two primary mechanisms, cycling-based aging and calendar-based aging. Cycling aging arises from repetitive charge–discharge cycles, enhancing solid-electrolyte interphase (SEI) growth, lithium plating, and particle fracture in electrode materials [10]. Calendar aging occurs during storage, driven by the storage temperature and state-of-charge (SoC), even in the absence of cycling [11]. Semi-empirical aging models, that capture these phenomena in the form of a simple analytical formulae which are fitted to experimental data, have been widely adopted to characterize these mechanisms [12–14]. These models provide valuable insights into the factors affecting battery lifetimes but are often limited by their reliance on specific operating conditions, thereby necessitating the collection of more comprehensive datasets to use for model calibration. The review of [15] summarizes well the various forms of semi-empirical models that have been used previously in the literature, as well as the challenges faced by semi-empirical aging models in recapitulating the complex degradation behavior of lithium-ion batteries.

Operational practices, including drive cycles, payloads, and charging strategies, significantly influence battery degradation in electric vehicles. High-current demands during acceleration and steep road grades exacerbate cycling aging, while extended periods of high SoC during storage intensify calendar aging. Studies by Jafari et al. [16] and Yang et al. [17] underscore the importance of optimizing operational profiles to mitigate these effects. Additionally, charging strategies significantly affect battery aging, particularly in HDCVs, where large battery packs are subject to frequent opportunity charging. For instance, immediate charging to full capacity, which exposes batteries to extended high SoC periods, has been seen to accelerate calendar aging [18]. In contrast, strategies such as delayed and minimum power charging have been shown to extend battery lifespan by maintaining lower SoC levels during idle periods [19].

[13] High-power opportunity charging, while essential for operational flexibility, contributes disproportionately to cycling degradation due to elevated stress due to the higher current amplitudes [20]. Optimizing these strategies requires balancing operational demands with long-term battery health, as was highlighted by the work of Pelletier et al. [21].

Despite considerable progress, gaps remain in understanding the long-term impacts of typical operational practices on battery system health in HDCVs. This study addresses this gap by incorporating detailed daily operational practices, including realistic driving cycles and diverse overnight charging strategies, to extend the current understanding of how these factors influence both cycling and calendar aging in HDCV batteries. Compared to existing studies [22–24], which have focused on specific drive cycles and which estimate degradation based on the total charge or energy throughput of the battery, this study highlights the nuanced interplay between battery chemistry and the operational demands. In particular, this study provides a comprehensive framework to estimate battery lifetimes within electrified vehicles by using Monte-Carlo-based simulations to account for the variability in road grade and seasonality conditions, which would be experienced by BETs in the real-world as they are driven along different regional routes. The stochasticity introduced by the Monte-Carlo procedure allows for the incorporation of uncertainty in the specific route experienced by an individual vehicle throughout its life, which is a feature that is seldom found in other simulators. Additionally, the study's focus on various charging strategies directly responds to gaps related to optimal charging practices, demonstrating their potential effectiveness in mitigating degradation. Furthermore, the findings reveal how high-power opportunity charging disproportionately contributes to battery aging, underscoring the need for infrastructure and operational strategies that prioritize battery longevity. The insights gained from our results offer actionable insights for fleet operators and policy makers aiming to balance performance, costs, and sustainability of electrified HDCVs.

Specifically, the models and methods developed in this work are applied to analyze the operations of drayage trucks as a case study. Drayage trucks are vehicles used to transport containers from ocean ports to inland consignee locations within the so-called "first mile" of freight logistics. In fact, drayage trucks travel several miles in a day, up to hundreds, as discussed in more detail later in this work.

The overall workflow of the research carried out is given in Fig. 1, and this paper is organized as follows: Section 2 outlines the methodology, including the vehicle model, a detailed lithium-ion battery model that integrates electrical, thermal, and aging dynamics, and the drayage truck daily operations modeling, which simulates daily activities of a typical drayage truck in a virtual environment, as well as model calibration procedures. Section 3 presents the results and discussion, covering model calibration, case study findings, and actionable insights to improve the performance and sustainability of battery BETs. Section 4 concludes the paper with a summary of key findings and implications for future work in electrified freight transport.

2. Methodology

This section outlines the modeling of the vehicle simulator, incorporating the electrical, thermal, and aging models for the Li-ion battery. This will be followed by a description of the approach used for modeling the daily activities of a typical drayage truck in a virtual environment.

2.1. Vehicle model

The vehicles used for analysis in this work are representative of heavy-duty Class-8 trucks available in U.S. markets. The energy-based modeling approach from [25] is followed for modeling the vehicle powertrain and the road load in a Matlab/Simulink virtual simulation environment.

2.1.1. Road-load model

A detailed road-load modeling approach is followed to model the resistive forces that are the aerodynamic drag, F_{aero}, rolling resistance, F_{roll}, grade, F_{grade} and inertial, F_{inertia}. The road load, F_{rl} acting on the vehicle along with the torque and speed required at the wheels are calculated using (1)–(7).

$$F_{\text{rl}} = F_{\text{aero}} + F_{\text{roll}} + F_{\text{grade}} + F_{\text{inertia}} \tag{1}$$

$$F_{\text{aero}} = \frac{1}{2}\rho_a C_d(\phi,\psi) A_f v^2 \tag{2}$$

$$F_{\text{roll}} = M g C_{rr}(T_{\text{tire}}(T_{\text{amb}}, v), v)\cos(\alpha) \tag{3}$$

$$F_{\text{grade}} = M g \sin(\alpha) \tag{4}$$

$$F_{\text{inertia}} = M_{eq}\frac{\mathrm{d}v}{\mathrm{d}t} \tag{5}$$

$$T_{\text{w}} = F_{\text{rl}} \cdot r_{\text{w}} \tag{6}$$

$$\omega_{\text{w}} = \frac{v}{r_{\text{w}}} \tag{7}$$

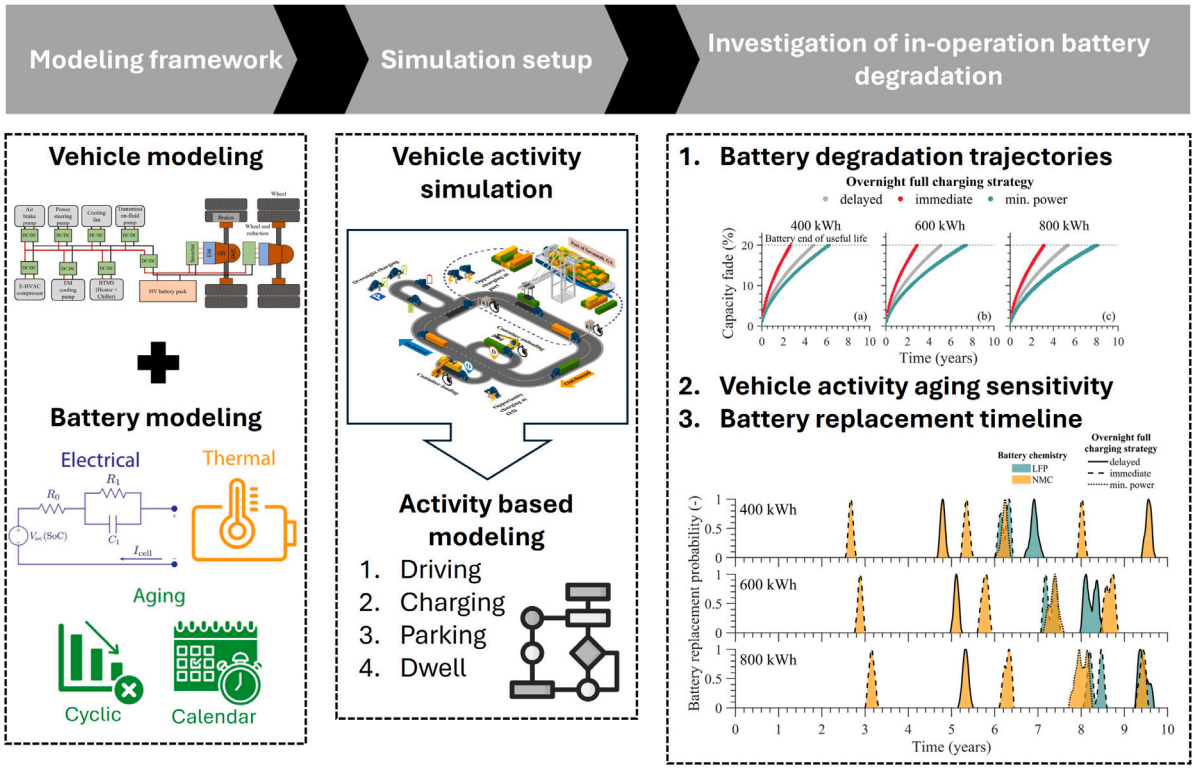

Fig. 1. Overall flow chart of developing the framework to analyze the battery degradation of in-operation battery electric HDCV in drayage application.

Table 1
Summary of electric drayage truck road load parameters.

Parameter	Value
Vehicle curb mass w/o battery pack (kg)	6930
Battery pack cell mass (kg)	$N_{\text{cell}} m_{\text{cell}}$
Battery pack w/o cell mass (kg)	$2.204 \cdot N_{\text{cell}} E_{\text{cell}}^{\text{nom}} + 27.146$
Frontal area (m^2)	10
Aerodynamic drag coefficient (–)	Function of truck configuration and yaw angle with wind
Rolling resistance coefficient (–)	Function of truck speed and tire shoulder temperature
Wheel radius (m)	0.483

where, ρ_a is the air density, T_{amb} is the ambient temperature, v is the vehicle speed, A_f is the frontal area, M is the vehicle weight, M_{eq} is the equivalent weight considering the powertrain rotational inertia, α is the road grade, g is the acceleration due to gravity, T_{w} is the total tractive wheel torque provided by the powertrain, ω_{w} is the wheel angular speed and r_{w} is the wheel radius. The aerodynamic drag coefficient, C_d depends on the truck configuration (bobtail, tractor–trailer, or tractor-flatbed trailer), ϕ, and the relative yaw angle between wind direction and vehicle heading, ψ. Similarly, the rolling resistance coefficient, C_{rr} is a function of tire shoulder temperature, T_{tire} and vehicle speed. First-order thermal dynamics for tires are also modeled which govern the tire shoulder temperature progression depending on the ambient temperature and vehicle speed [26]. The summary of vehicle road load parameters is given in Table 1

In the above table, N_{cell} is the total number of cells in the battery pack, m_{cell} is the mass of individual cells, and $E_{\text{cell}}^{\text{nom}}$ is the nominal energy of the cells in kWh. The total vehicle weight, M is given as the sum of vehicle curb mass without the battery pack, the battery pack mass which depends on cell chemistry and nominal energy, as well as the cargo and container-trailer mass. The equation used to determine the battery pack mass is obtained from [27]

2.1.2. Powertrain model

The powertrain of the battery electric truck as illustrated in Fig. 2 is a tandem e-axle configuration and is based on the data available on the Kenworth 6 × 4 T680E [28]. The e-axle is composed of an electric motor (EM) and inverter along with an integrated 3-speed gearbox and differential gear. EM efficiency is modeled using a performance map, while gearbox and differential have fixed efficiencies. The combined total power of both the e-axles is 500 kW. In addition, different auxiliary components such as the Electric-Heating, Ventilation, and Air Conditioning (E-HVAC), Battery Thermal Management System (BTMS), EM cooling pump, air brake pump, power steering pump, cooling fan, and transmission-fluid pump are modeled using a duty-cycle based modeling method as described in [29]. The auxiliary component power draw is dependent on ambient temperature conditions which causes significant variation in auxiliary power consumption throughout the year due to seasonal variations. The model equations for the electric truck powertrain are given below:

$$T_{\text{w}} = T_{\text{ax}} + T_{\text{br}} \tag{8}$$

$$T_{\text{em}} = \frac{T_{\text{ax}}}{n_e \cdot \lambda_{\text{gb,i}} \cdot \lambda_{\text{fd}} \cdot \lambda_{\text{we}}} \eta_{\text{gb,i}}^{\gamma} \cdot \eta_{\text{fd}}^{\gamma} \cdot \eta_{\text{we}}^{\gamma} \begin{cases} \gamma = 1, & T_{\text{ax}} < 0 \\ \gamma = -1, & T_{\text{ax}} \geq 0 \end{cases} \tag{9}$$

$$\omega_{\text{em}} = \omega_{\text{w}} \cdot \lambda_{\text{gb,i}} \cdot \lambda_{\text{fd}} \cdot \lambda_{\text{we}} \tag{10}$$

$$P_{\text{em}} = T_{\text{em}} \cdot \omega_{\text{em}} \cdot \eta_{\text{em}}^{\gamma}(T_{\text{em}}, \omega_{\text{em}}) \begin{cases} \gamma = 1, & T_{\text{em}} < 0 \\ \gamma = -1, & T_{\text{em}} \geq 0 \end{cases} \tag{11}$$

$$I_{\text{pack}} = \frac{n_e \cdot P_{\text{em}} + P_{\text{aux}}(T_{\text{amb}})}{V_{\text{pack}}} \tag{12}$$

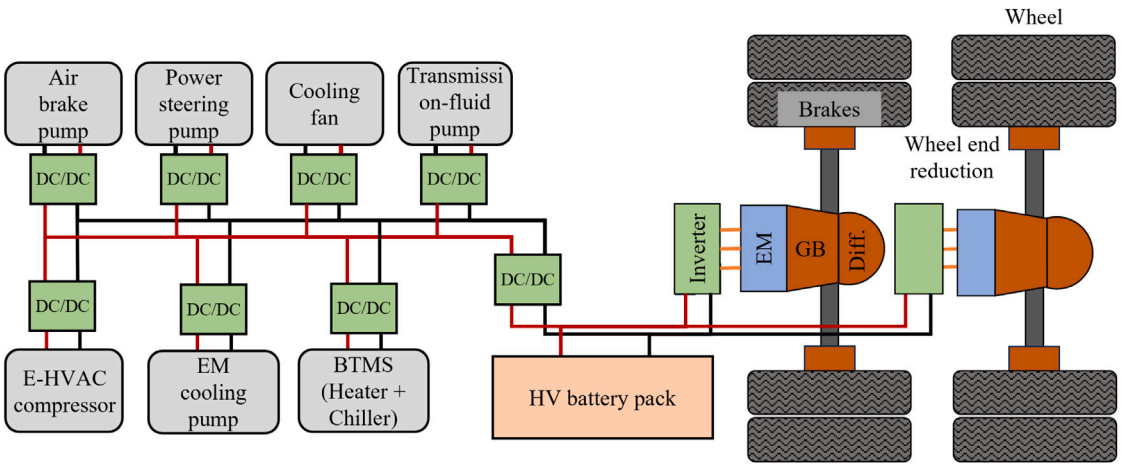

Fig. 2. Schematic of the battery electric truck powertrain. GB: gear box; Diff.: differential gear; DC/DC: converters; LV: low voltage; EM: electric motor.

where, T_{ax} is the total axle torque and T_{br} is the total brake torque. $T_{em}, \omega_{em}, P_{em}$ and η_{em} are the EM torque, angular speed, electrical power and efficiency, respectively. n_e (=2) is the number of e-axles, with $\lambda_{gb,i}$ and $\eta_{gb,i}$ are the gear reduction and gear efficiency of ith gear of the gearbox, respectively, while λ_{fd} and η_{fd} are the gear reduction and efficiency of the final drive reduction, respectively, and, λ_{we} and η_{we} being the gear reduction and efficiency of the wheel end reduction, respectively. I_{pack} and V_{pack} are the current and terminal voltage of the high-voltage Li-ion battery pack, respectively. $P_{aux}(T_{amb})$ is the total power drawn from the battery pack due to all electrical accessories.

For further explanation on the detailed road load and powertrain model, and the influence of seasonal variations on vehicle energy consumption interested readers are encouraged to read our previous work [30].

2.2. Lithium-ion battery model

To capture the capabilities of the electrified HDCVs during operation, the dynamics of the battery pack are modeled by assumption of homogeneous scaling of the dynamics of a single battery-cell. The pack voltage V_{pack} and the pack current I_{pack} are thus related to their cell-level counterparts V_{cell} and I_{cell}, respectively, through the following relations:

$$V_{pack}^{(c)} = N_{series}^{(c)} \cdot V_{cell}^{(c)} \tag{13}$$

$$I_{pack}^{(c)} = N_{parallel}^{(c)} \cdot I_{cell}^{(c)} \tag{14}$$

The superscript $c \in \{\text{NMC, LFP}\}$ denotes the battery chemistry of the cells in the pack, $N_{series}^{(c)}$ denotes the number of cells connected in series and $N_{parallel}^{(c)}$ denotes the number of cells connected in parallel. As the nominal voltage $V_{cell,nom}$ and nominal capacity (in units of ampere-hours) Q_{cell}^{nom} of each cell chemistry is different, the number of cells needed to be placed in series and parallel also varies depending on the cell chemistry, the desired voltage $V_{pack,nom}$, and the desired energy (in units of Watt-hours) $E_{pack,nom}$ of the pack. Specifically, the number of cells placed in series or in parallel are computed according to [31],

$$N_{series}^{(c)} = \frac{V_{pack,nom}}{V_{cell,nom}^{(c)}} \tag{15}$$

$$N_{parallel}^{(c)} = \frac{E_{pack,nom}^{(c)}}{V_{pack,nom}^{(c)} \cdot Q_{cell,nom}^{(c)}} \tag{16}$$

The total number of cells contained in the pack is $N_{cells} = N_{series} \cdot N_{parallel}$. In the following sections, the models used to capture the electrical and thermal dynamics of the battery cells in the pack are first introduced. A separate temperature model for the temperature of the pack housing is introduced to capture the thermal interactions between the cell and the pack housing. The degradation models which capture the cycling and calendar aging of the battery cells are then introduced and the procedure by which they are calibrated to experimental data is explained. A schematic of the overall battery pack model, including the sub-models and their interactions with one another, is shown in Fig. 3.

2.2.1. Battery cell electrical model

A first-order equivalent-circuit model (ECM) is used to capture the electrical dynamics of a single cell within the pack. The first-order ECM model contains an RC branch whose voltage $V_{RC}^{(c)}(t)$ has dynamics described by [32],

$$\frac{\mathrm{d}}{\mathrm{d}t} V_{RC}^{(c)} = -\frac{1}{\tau_1^{(c)}(\text{SoC})} V_{RC} + \frac{1}{C_1^{(c)}(\text{SoC})} I_{cell}(t) \tag{17}$$

where $I_{cell}(t)$ is the applied current, $\tau_1(\text{SoC}) = R_1(\text{SoC}) \cdot C_1(\text{SoC})$ is the voltage relaxation timescale, $C_1(\text{SoC})$ is the RC branch capacitance. The state-of-charge (SoC) of the battery with a nominal capacity (units: Ah) of $Q_{cell}^{nom,(c)}$ is obtained from Coulomb counting,

$$\frac{\mathrm{d}}{\mathrm{d}t} \text{SoC}(t) = -\frac{1}{3600 \cdot Q_{cell,nom}^{(c)}} I_{cell}(t) \tag{18}$$

The factor of 3600 in the denominator of (18) is a conversion factor from hours to seconds. The system output is the cell terminal voltage, which for the NMC battery chemistry is computed according to,

$$V_{cell}^{model,NMC}(t) = V_{oc}^{NMC}(\text{SoC}) - I_{cell}(t) \cdot R_0^{NMC}(\text{SoC}) - V_{RC}^{NMC}(t) \tag{19}$$

Here, $R_0^{(c)}(\text{SoC})$ denotes the high-frequency resistance which captures the instantaneous response of the battery to changes in the input current.

On the other hand, for the LFP battery chemistry, the phenomenon of *hysteresis* is known to play a more dominant role [33]. Hysteresis in batteries is an effect wherein the response of the battery on discharge is significantly different than its response on charge. Importantly, hysteresis is distinct from polarization as hysteresis may be observed regardless of the magnitude of the current, while polarization vanishes as the current magnitude is reduced. As such, for LFP, two modifications to the electrical model are made to capture hysteresis following [34]. First, the parameters of the RC branch dynamics (17) are made dependent on the directionality of current, $\tau_1^{LFP}(\text{SoC}) \rightarrow \tau_1^{LFP}(\text{SoC}, \text{sgn}(I))$ and $C_1^{LFP}(\text{SoC}) \rightarrow C_1^{LFP}(\text{SoC}, \text{sgn}(I))$, where the signum function is defined as,

$$\text{sgn}(x) = \begin{cases} +1, & x \geq 0 \\ -1, & \text{otherwise} \end{cases} \tag{20}$$

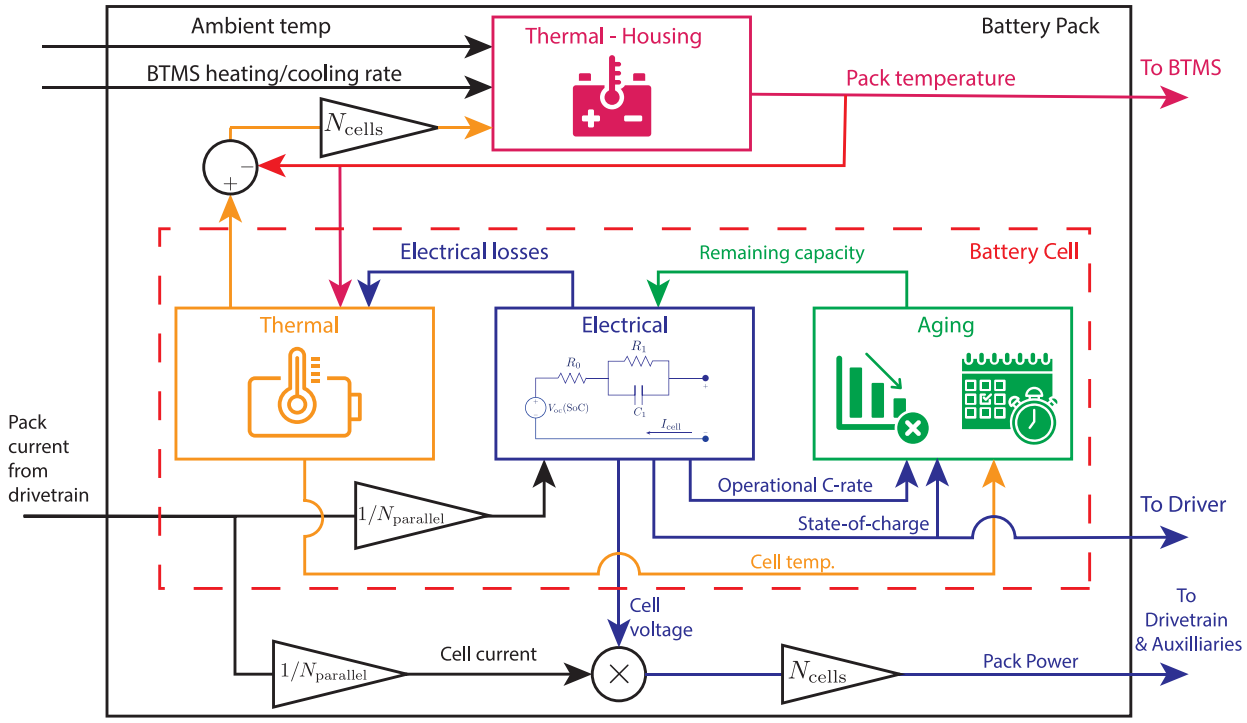

Fig. 3. Schematic of the high-voltage battery pack model. The model is comprised of a battery cell model that captures the electrical, thermal, and long-term aging behavior (in the dashed red box). The battery cell output is up-scaled to the pack output using (13) and (14). During operation, the cells incur Joule losses causing a change to their temperature. All the cells are enclosed within and exchange heat with the housing of the pack according to (24). The housing exchanges heat with the ambient environment and is additionally cooled/heated externally by a battery thermal management system (BTMS). The BTMS monitors the pack housing temperature and the input cooling/heating rate is determined according to (25). As the battery is used, it degrades at a rate that depends on the temperature experienced by the cell and the operational C-rate. This degradation alters the capacity, which affects the dynamics of the battery state-of-charge.

Second, an instantaneous hysteresis state $s(t)$ whose dynamics are described by,

$$s(t) = \begin{cases} \text{sgn}[I_{\text{cell}}(t)], & |I_{\text{cell}}(t)| > 0 \\ s(t^-), & \text{otherwise} \end{cases} \tag{21}$$

is added, where t^- denotes an infinitesimal time point before time t. Given these two modifications, the modified cell terminal voltage for the LFP chemistry is,

$$V_{\text{cell}}^{\text{model,LFP}}(t) = V_{\text{oc}}^{\text{LFP}}(\text{SoC}) + M_0(\text{SoC})s - I_{\text{cell}}(t) \cdot R_0^{\text{LFP}}(\text{SoC}) - V_{RC}^{\text{LFP}}(t) \tag{22}$$

where $M_0(\text{SoC})$ is the instantaneous hysteresis voltage [35].

The model's SoC-dependent parameters, $R_0^{(c)}(\text{SoC})$, $\tau_1^{(c)}(\text{SoC})$, $C_1^{(c)}(\text{SoC})$ are obtained from calibration to experimental data for each battery chemistry c. The calibration and model validation procedures for both chemistries, along with their respective results, are presented in Appendix.

2.2.2. Battery cell thermal model

As the battery pack is operated, electrical losses cause a temperature change within the cells. This behavior is captured with the following lumped-parameter model [36,37],

$$C_{\text{cell}} \frac{\text{d}}{\text{d}t} T_{\text{cell}} = I_{\text{cell}}(t) \left[V_{\text{oc}}^{(c)}(\text{SoC}) - V_{\text{cell}}^{(c)}(t) \right] + \frac{T_{\text{housing}} - T_{\text{cell}}}{R_{\text{housing,cell}}} \tag{23}$$

where C_{cell} is the effective thermal coefficient of the cell. The first term on the right-hand side of (23) represents the Joule losses that occur within the cell during operation, while the second term is the effective heat exchange between a single cell and the surrounding housing characterized by a heat-exchange resistance $R_{\text{housing,cell}}$. The thermal model parameters C_{cell}, $R_{\text{housing,cell}} \in \mathbb{R}$ are assumed to be independent of the SoC of the cells in the pack. Their values are obtained by calibrating this model to available experimental temperature data (see Appendix for further details).

2.2.3. Pack housing thermal model

The thermal dynamics of the battery pack housing is modeled separately to capture the collective effects of heating from all the cells enclosed within. The battery pack housing is assumed to have a thermal capacity C_{housing} and its temperature dynamics follow [38],

$$C_{\text{housing}} \frac{\text{d}}{\text{d}t} T_{\text{housing}} = N_{\text{cells}} \cdot \frac{T_{\text{cell}} - T_{\text{housing}}}{R_{\text{housing,cell}}} + \frac{T_{\text{amb}} - T_{\text{housing}}}{R_{\text{amb,housing}}} + \dot{Q}_{\text{TMS}} \tag{24}$$

where the first term on the right-hand side represents the thermal contributions of all the enclosed cells to heating the pack, the second term represents the exchange of heat between the pack housing and the ambient environment characterized by the thermal equivalent resistance $R_{\text{amb,housing}}$. Similar to the cell-level temperature model, the parameters C_{housing} and $R_{\text{amb,housing}}$ are considered to be independent of the state of the cells in the pack. The rejection capabilities of the thermal management system (TMS), $\dot{Q}_{\text{TMS}}$ are determined by a simple controller with a discrete set of outputs:

$$\dot{Q}_{\text{TMS}} = \begin{cases} 0, & 15\ ^\circ\text{C} \le T_{\text{housing}} \le 30\ ^\circ\text{C} \\ 50\ \text{kW}, & T_{\text{housing}} < 15\ ^\circ\text{C} \\ 100\ \text{kW}, & T_{\text{housing}} < 15\ ^\circ\text{C for longer than 10 min} \\ -50\ \text{kW}, & T_{\text{housing}} > 30\ ^\circ\text{C} \\ -100\ \text{kW}, & T_{\text{housing}} > 30\ ^\circ\text{C for longer than 10 min} \end{cases} \tag{25}$$

Negative values of $\dot{Q}_{\text{TMS}}$ represent cooling of the pack housing while positive values represent heating. The temperature controller monitors the pack temperature and operates to keep the pack housing temperature within the acceptable range $15\ ^\circ\text{C} \le T_{\text{housing}} \le 30\ ^\circ\text{C}$. The heat rejection capabilities of the TMS were chosen so that across all of the routes that trucks will drive on in the operation region, a 400 kWh battery pack would be able to reach the acceptable temperature window within 30 min when initialized from the coldest or the

hottest conditions attained in the given region. Equation (25) therefore reflects a representative TMS energy scaling assumption and should be interpreted as a bounding estimate of capabilities rather than a prescriptive hardware specification. The thermal rejection capabilities of the TMS, $\dot{Q}_{\text{TMS}}$, are related to the amount of power requested from the battery $P_{\text{TMS,batt}}$ to support TMS operation by the coefficient of performance [38],

$$\text{COP} = \begin{cases} 3, & \dot{Q} < 0 \\ 4, & \dot{Q} > 0 \end{cases} \tag{26}$$

according to $|\dot{Q}_{\text{TMS}}| = \text{COP} \cdot P_{\text{TMS,batt}}$.

2.2.4. Cycling and calendar aging model

To capture the capacity fade behaviors of lithium-ion batteries, particularly under cycling-based and calendar-based aging conditions, semi-empirical models are used. By incorporating both cycling and calendar effects, semi-empirical models are considered an important tool that provides an ideal trade-off between model complexity and computation time and enables forecasting of battery lifespan in real-world applications [13,39,40].

The experimental capacity fade due to cycling-based aging is defined to be the relative ratio [12],

$$Q^{\text{data}}_{\text{loss,cyc}}(\text{Ah}; T_{\text{cell}}, I_C) = \frac{Q^{\text{data}}_{\text{cell}}(\text{Ah}=0; T_{\text{cell}}, I_C) - Q^{\text{data}}_{\text{cell}}(\text{Ah}; T_{\text{cell}}, I_C)}{Q^{\text{data}}_{\text{cell}}(\text{Ah}=0; T_{\text{cell}}, I_C)} \tag{27}$$

of the measured cell capacity $Q^{\text{data}}_{\text{cell}}(\text{Ah}; T_{\text{cell}}, I_C)$ at a particular value of the ampere-hour (Ah) throughput,

$$\text{Ah} = \frac{1}{3600}\int_0^t |I(s)|\mathrm{d}s \tag{28}$$

and the capacity of the fresh cell at the beginning of life, $Q^{\text{data}}_{\text{cell}}(\text{Ah} = 0; T_{\text{cell}}, I_C)$, prior to it ever being used. The Ah-throughput (28) measures the total amount of charge that has passed through the battery from the start of its life ($t = 0$) up to a time t. Experimental measurements of the capacity fade can be collected through an *aging campaign* which consists of applying a prescribed current input profile $I^{\text{exp}}_{\text{pack}}(t)$, often characterized by an operational C-rate

$$I_C = \frac{I_{\text{cell}}}{Q^{\text{nom}}_{\text{cell}}} \tag{29}$$

to discharge the cell, followed by a recharge back to the initial state, in a controlled ambient temperature environment. This cycle is repeated many times over to mimic the operation of the battery. After a number of cycles set by the experimental design, a set of reference performance tests (RPTs) are performed on the cell to check its status. One of these is a capacity test in which a cell is charged to the full upper cutoff voltage, and then slowly discharged (typically at a C-rate of $C/3$ or lower) until the cell voltage reaches the bottom cutoff voltage. The total Ah-throughput measured during this discharge is considered the capacity of the cell at that reference test $Q^{\text{data}}_{\text{cell}}(\text{Ah}; T_{\text{cell}}, I_C)$.

To characterize cycling-based aging measured by (27), the following empirical degradation model is proposed,

$$Q^{\text{model},(c)}_{\text{loss,cyc}}(\text{Ah}, T_{\text{cell}}, I_C; \theta^{(c)}_{\text{cyc}}, \zeta^{(c)}_{\text{cyc}}) = \sigma^{\text{model},(c)}_{\text{cyc}}(T_{\text{cell}}, I_C; \theta^{(c)}_{\text{cyc}}) \cdot (\text{Ah})^{\zeta^{(c)}_{\text{cyc}}} \tag{30}$$

that is a power-law in the total Ah-throughput of the cell with an exponent of $\zeta^{(c)}_{\text{cyc}}$. This form for an empirical degradation model was initially proposed by Serrao et al. [41]. The degree of capacity fade is scaled by a *severity factor function* $\sigma^{\text{model},(c)}_{\text{cyc}}$ which, itself, is a function of the *stress factors*. For cycling-based aging, the stress factors considered here are cell temperature T_{cell} and the operational C-rate I_C. The parameters $\theta^{(c)}_{\text{cyc}}$ are calibrated using experimental aging campaign data through a procedure described in Section 2.2.5.

Similarly, calendar-based aging is collected from aging campaigns where a battery is stored at rest under a specific storage SoC and at controlled ambient conditions. Reference performance tests are periodically performed on the stored battery every set number of days and a capacity measurement $Q^{\text{data}}_{\text{cell}}(t_{\text{store}}; T_{\text{cell}}, \text{SoC}_{\text{store}})$ is obtained. The experimentally measured capacity fade due to calendar aging, analogously to (27), is defined according to [13],

$$Q^{\text{data}}_{\text{loss,cal}}(t_{\text{store}}; T_{\text{cell}}, \text{SoC}_{\text{store}}) = \frac{Q^{\text{data}}_{\text{cell}}(t_{\text{store}}=0; T_{\text{cell}}, \text{SoC}_{\text{store}}) - Q^{\text{data}}_{\text{cell}}(t_{\text{store}}; T_{\text{cell}}, \text{SoC}_{\text{store}})}{Q_{\text{cell}}(t_{\text{store}}=0; T_{\text{cell}}, \text{SoC}_{\text{store}})} \tag{31}$$

To characterize the experimental calendar aging data (31), the following empirical degradation model is proposed,

$$Q^{\text{model},(c)}_{\text{loss,cal}}(t_{\text{store}}, T_{\text{cell}}, \text{SoC}_{\text{store}}; \theta^{(c)}_{\text{cal}}, \zeta^{(c)}_{\text{cal}}) = \sigma^{\text{model},(c)}_{\text{cal}}(T_{\text{cell}}, \text{SoC}_{\text{store}}) \cdot (t_{\text{store}})^{\zeta^{(c)}_{\text{cal}}} \tag{32}$$

The storage time measures the total amount of time that the battery is at rest and no current is flowing:

$$t_{\text{store}} = \int \mathrm{d}t \begin{cases} 1, & |I(t)| = 0 \\ 0, & \text{otherwise} \end{cases} \tag{33}$$

The severity factor function $\sigma^{\text{model},(c)}_{\text{cal}}(T_{\text{cell}}, \text{SoC}_{\text{store}})$ is assumed to depend on the storage temperature and storage SoC, in the case of calendar-based aging. The calibration procedure for the calendar aging model follows a similar procedure outlined in Section 2.2.5.

In general, when left unmitigated, small variations arising from manufacturing differences between cells in a battery pack are known to induce higher levels of aging in the pack overall [42,43]. To simplify the analysis, it is assumed that control algorithms within the onboard battery management system (BMS) minimize instantaneous cell-to-cell variation during operation, thereby allowing the effects of this variation to be neglected [44].

2.2.5. Aging model calibration

In this section, the calibration of the empirical aging models described in Section 2.2.4 to experimental LIB data is discussed. For clarity and concreteness, the calibration of the cycling-based degradation model is discussed first here. The differences between the cycling-based degradation model and calendar-based degradation models are then discussed.

Let the base cycling-based degradation model have the form,

$$Q^{\text{model,base}}_{\text{loss,cyc}}(\text{Ah}_j; \sigma_{\ell k}, \zeta) = \sigma_{\ell k} \cdot \left(\text{Ah}_j\right)^{\zeta} \tag{34}$$

where Ah_j, $j = 1, \ldots, N_{\text{Ah}}$ denotes the Ah throughput at the jth capacity test in a cycling aging data set and $\sigma_{\ell k} = \sigma((T_{\text{cell}})_\ell, (I_C)_k)$ denotes the values of the severity factor function corresponding to the ℓth cell temperature and kth operating C-rate conditions.

Given the base model (34), the general procedure used to calibrate the aging models and their parameters here[2]:

1. Using least-squares, the value of the exponent ζ_{cyc} that minimizes the total error for all tested stress factor values is determined:

$$\zeta^*_{\text{cyc}} = \arg\min_{\zeta_{\text{cyc}}} \times \left\{ \sum_{\ell=1}^{N_{T_{\text{cell}}}} \sum_{k=1}^{N_{I_C}} \left(\min_{\sigma_{\ell k}} \sum_{j=1}^{N_{\text{Ah}}} \left[Q^{\text{model,base}}_{\text{loss,cyc}}(\text{Ah}_j; \sigma_{\ell k}, \zeta_{\text{cyc}}) - Q^{\text{data}}_{\text{loss,cyc}}(\text{Ah}_j; (T_{\text{cell}})_\ell, (I_C)_k) \right]^2 \right) \right\} \tag{35}$$

2. Having obtained the optimal exponent value in the previous step, find the optimal values for the severity factor function for each combination of cell temperature and operating C-rate

[2] This procedure must be repeated for each chemistry explained earlier. To keep the notation clear, the chemistry dependence from the symbols is suppressed from this section onwards.

condition that minimizes the sum-of-squares error between the base model and the data,

$$\sigma^*_{\ell k} = \arg\min_{\sigma_{\ell k}} \left\{ \sum_{j=1}^{N_{\text{Ah}}} \left[Q^{\text{model,base}}_{\text{loss,cyc}}(\text{Ah}_j; \sigma_{\ell k}, \zeta^*_{\text{cyc}}) - Q^{\text{data}}_{\text{loss,cyc}}(\text{Ah}_j; (T_{\text{cell}})_\ell, (I_C)_k) \right]^2 \right\} \tag{36}$$

3. Propose a parameterized functional representation $\sigma^{\text{model}}_{\text{cyc}}(T_{\text{cell}}, I_C; \theta_{\text{cyc}})$ that characterizes the obtained severity factor function values, where θ_{cyc} is the parameter vector.
4. Find the values of the parameter vector θ_{cyc} by applying least-squares equation on the severity factor values obtained in Step 2

$$\theta^*_{\text{cyc}} = \arg\min_{\theta_{\text{cyc}}} \left\{ \sum_{\ell=1}^{N_T} \sum_{k=1}^{N_{I_C}} \left[\sigma^{\text{model}}_{\text{cyc}}((T_{\text{cell}})_\ell, (I_C)_k; \theta_{\text{cyc}}) - \sigma^*_{\ell k} \right]^2 \right\} \tag{37}$$

The calibrated cycling aging model is then

$$Q^{\text{model}}_{\text{loss}}(\text{Ah}, T_{\text{cell}}, I_C; \theta^*_{\text{cyc}}, \zeta^*_{\text{cyc}}) = \sigma^{\text{model}}_{\text{cyc}}(T_{\text{cell}}, I_C; \theta^*_{\text{cyc}}) \cdot (\text{Ah})^{\zeta^*_{\text{cyc}}} \tag{38}$$

The calibration process for calendar-based degradation models proceeds in a similar manner as above, with the primary difference being that the storage time is used instead of Ah-throughput, $\text{Ah} \to t_{\text{store}}$, and the severity factor function is dependent on the cell temperature T_{cell} and storage $\text{SoC}_{\text{store}}$, the relevant severity factors for this degradation mode.

2.2.6. Integrating aging models into dynamic simulations

Following the approach proposed in [45], a differential of both the cycling and calendar aging-models is carried out, thereby obtaining the corresponding dynamical equations in time describing the degradation of the battery,

$$\frac{\text{d}}{\text{d}t} Q^{\text{model}}_{\text{cyc}} = \sigma^{\text{model}}_{\text{cyc}}(T_{\text{cell}}, I_C) \cdot \zeta^{(\text{c})}_{\text{cyc}} \cdot (\text{Ah})^{\zeta^{(\text{c})}_{\text{cyc}} - 1} \cdot I_{\text{cell}}(t) \tag{39}$$

$$\frac{\text{d}}{\text{d}t} Q^{\text{model}}_{\text{cal}} = \sigma^{\text{model}}_{\text{cal}}(T_{\text{cell}}, \text{SoC}_{\text{store}}) \cdot \zeta^{(\text{c})}_{\text{cal}} \cdot (t_{\text{store}})^{\zeta^{(\text{c})}_{\text{cal}} - 1} \tag{40}$$

At a given instant t, the relevant degradation mode is determined by the current value into the pack:

$$\frac{\text{d}}{\text{d}t} Q^{\text{model}}_{\text{loss,tot}} = \begin{cases} \frac{\text{d}}{\text{d}t} Q^{\text{model}}_{\text{loss,cyc}}, & |I_{\text{pack}}(t)| \neq 0 \\ \frac{\text{d}}{\text{d}t} Q^{\text{model}}_{\text{loss,cal}}, & |I_{\text{pack}}(t)| = 0 \end{cases} \tag{41}$$

The dynamic aging models (39)–(40) and (41) is integrated into the vehicle model in Simulink and is time-evolved with the other components of the vehicle model. Notably, as sufficiently small time steps are used in the integration of the dynamical equations of the vehicle and battery model, $\Delta t_{\text{sim}} = 10^{-1}$ s, the change in the stress factors will also be small in between subsequent simulation time steps. As such, virtual-time constructions [13] are not needed to map the degradation from one time step to the next.

Note that the degradation submodels are implemented in a modular form within the simulation framework, such that the calibrated parameter sets used here may be directly replaced with alternative, cell-specific, values without modification to the overall modeling structure.

In addition, to enable efficient integration of the degradation dynamics within the vehicle simulation framework, the aging models are applied under the assumption of homogeneous current distribution across all parallel cell groups, consistent with common practice in pack-level lifetime studies. This implicitly assumes that the BMS is effective in mitigating cell-to-cell variations in state-of-charge and impedance during operation. While this approximation enables tractable simulation of long-term pack usage, it idealizes real pack behavior where manufacturing variation, local thermal gradients, and unequal impedance growth may lead to selective overstress of the weakest cells. As such, the resulting degradation trajectories should be interpreted as representative of an upper-bound lifetime scenario under ideal balancing and thermal regulation.

2.3. Charger modeling

As the trucks operate throughout the day, charging is required both mid-mission and overnight at the fleet depot. To model this process, a charger model is developed that captures interactions with the grid, internal charger losses, and the interface between the charger and the battery.

The maximum power delivered by the charger to the battery $P_{\text{charge,max}}$ (in kW) is determined by the battery SoC according to the following piecewise relation:

$$\frac{P_{\text{charge,max}}}{P_{\text{charger,rated}}} = \begin{cases} \dfrac{20}{P_{\text{charger,rated}}}, & \text{SoC} < \text{SoC}^{\text{min}}_{\text{max win}} \\ 1, & \text{SoC}^{\text{min}}_{\text{max win}} \leq \text{SoC} < \text{SoC}^{\text{max}}_{\text{max win}} \\ \left(\dfrac{1 - \text{SoC}}{1 - \text{SoC}^{\text{max}}_{\text{max win}}} \right) \exp\left(B \left[1 - \dfrac{\text{SoC}}{\text{SoC}^{\text{max}}_{\text{max win}}} \right] \right), & \text{SoC}^{\text{max}}_{\text{max win}} \end{cases} \tag{42}$$

A window of SoC values – bounded by a lower limit $\text{SoC}^{\text{min}}_{\text{max win}}$ and an upper limit $\text{SoC}^{\text{max}}_{\text{max win}}$ – within which the charger can deliver its rated power $P_{\text{charger,rated}}$ is defined. Below this window, the battery trickle charges at a constant low power level at a fixed power of 20 kW. Above this window, the maximum allowable charging power decreases exponentially, ultimately reaching zero as the battery SoC approaches 100%.

While (42) describes the maximum allowable charging power, real-world inefficiencies – as well as power consumed by auxiliary components within the charger unit – reduce the actual power delivered to the battery [46]. To account for these losses, the measured efficiency data from the ENERGY STAR certification program for Electric Vehicle Supply Equipment is utilized [47]. In particular, the "Star Charge DC2400AN06702" is used as a representative DC fast charger and its output efficiency as a fraction of the rated power is applied [48].

The charging model is integrated with the battery pack model described in Section 2.2. During charging events, the charger uses the battery's SoC to determine the power input according to (42) minus losses (due to the output efficiency) to the battery. By combining the models in this way, the charging simulation consistently captures the battery polarization response during the charging event. To keep the battery model close to its calibrated operating range, the maximum charging current is capped at 1.5 C. This restricts the simulations to conditions under which polarization and plating-driven deviations from ideal charge tracking remain a higher-order effect. Extension to fast-charge (> 2 to 3 C) regimes would require additional calibration data (for all three submodels), which are beyond the scope of this study. The 1.5 C cap scales naturally with the size of the battery pack and is applied to both chemistries considered in this work.

2.4. Drayage truck daily operations modeling

The daily operations of the drayage trucks are modeled in this work using the activity-based model (ABM) [49]. The ABM framework allows to model daily electric drayage truck use as well as different charging strategies that can be employed for overnight charging by defining four possible truck activities: driving, dwelling, parking, and recharging. Fig. 4 illustrates an idealized drayage truck operation based on the drayage description provided in [50]. Import containers are transported by drayage trucks from an ocean port to consignee locations during outbound trips. To maximize driver productivity and improve truck utilization, after delivering the import containers, the trucks return to the port via inbound trips with export containers picked-up from the shipper locations. It is assumed here that all containers are the same size (40 ft), allowing for containers to be transported on the same chassis. This is not always the case, as containers can vary in size (20 ft or 40 ft), which may require a chassis swap and additional trips to

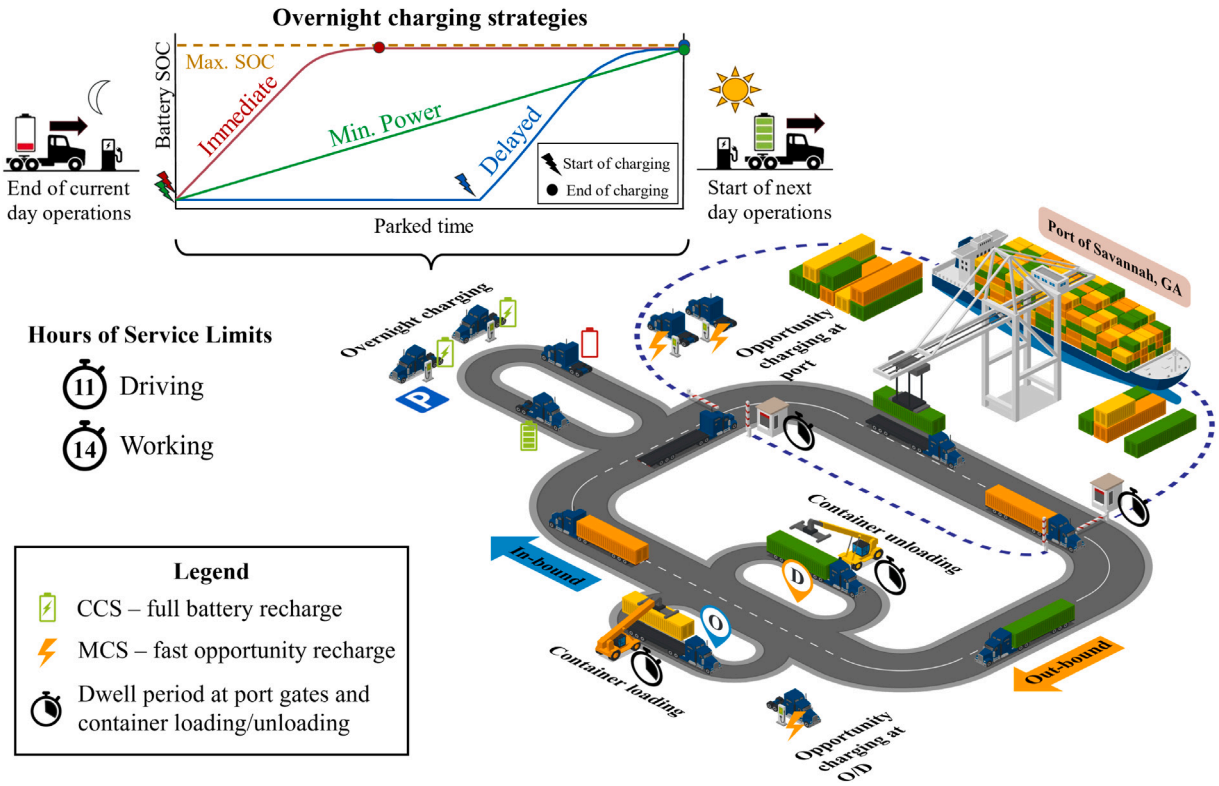

Fig. 4. Pictorial representation of drayage operations. Figure created with an open-sourced graphic designer. (https://icograms.com).

the chassis yard. While perfectly aligning import and export shipment assignments is rarely possible, as orders can be canceled or created unexpectedly throughout the day, in this analysis it is assumed that after making the import container delivery, the next export container is readily available for pick-up from a nearby location.

Furthermore, there will also be certain trips made from (to) the truck depot to (from) the port at the start (end) of the day. However, these trips would be short in distance as truck depots are in the port region. Thus, these trips are not considered in this work. The month-wise in-bound and out-bound routes origins and destinations (ODs) for drayage trucks operating at the Port of Savannah, GA are obtained using the process described in [51], which utilizes the freight movement information collected using the Streetlight data. Further, by utilizing the weight station data for Class-8 vehicles from a Traffic Monitoring Analysis System station located near the port gates, the drayage truck weight distribution statistics are determined for assigning the loaded trucks' cargo weight during the inbound and outbound trips.

In addition to driving trips from/to port, the drayage trucks spend considerable working time idling while waiting in queues at port gates as well as waiting for the container to be loaded/unloaded at the port and customer locations [52]. The truck turn time at ports, which consists of time spent in queue as well as the time for loading and unloading can range from a few minutes to a couple of hours. To incorporate this in the daily activity modeling of drayage trucks, the dwelling periods (in minutes) are randomly assigned based on uniform distributions for different processes as follows:

$$\begin{aligned} t_{\text{ContainerLoading}} &\sim U(30,60) \\ t_{\text{ContainerUnloading}} &\sim U(30,60) \\ t_{\text{PortTurnTimeLoading}} &\sim U(30,120) \\ t_{\text{PortTurnTimeUnloading}} &\sim U(30,90) \end{aligned} \tag{43}$$

Drayage truck drivers' daily operations are constrained by Hours of Service (HOS) regulations, which limit driving time to 11 h and total working time to 14 h. Once either of the two HOS limits is surpassed, the driver is required to take a mandatory 10 h of off-duty time [53].

Most ports in the U.S. typically operate during the day (7 am to 5 pm), which means that drayage truck activity occurs primarily during the day, while the off-duty period takes place during overnight parking. Battery electric trucks can be fully recharged during this time using Combined Charging Systems (CCS) chargers; however, different overnight charging strategies can be used to ensure a fully charged battery at the start of the next day's operations. This work considers three overnight charging strategies: immediate, delayed, and minimum power.

In the immediate overnight charging strategy, charging begins as soon as the electric truck is connected to the charger. The charging time to reach full battery SoC varies depending on the charge needed and the battery size. Once fully charged, the system stops charging and the battery rests for the rest of the night. The charging process starts later in the delayed charging strategy, allowing the battery to rest initially after being plugged in. Charging begins when the time left before the next day's operations matches the required charging time. The key difference between the two strategies is the battery's SoC while parked. In the immediate strategy, the battery remains at maximum SoC, while in the delayed strategy, the resting SoC is significantly lower. The impact of resting SoC on battery degradation due to calendar effects will be analyzed later. Both strategies use CCS chargers with a power limit of 150 kW.

A more effective approach to mitigating battery degradation due to calendar aging is to employ a minimum-power overnight charging strategy. In this approach, the battery is fully charged using low power, ensuring that the total charging time matches the overnight parking duration. On weekends, the charging power is further reduced to account for daytime parking on Saturday and Sunday. The top plot of Fig. 4 shows the battery SoC profile resulting from these overnight charging strategies during the parked period. As mentioned earlier, the drayage trucks are not in operation during the night due to the port closure,

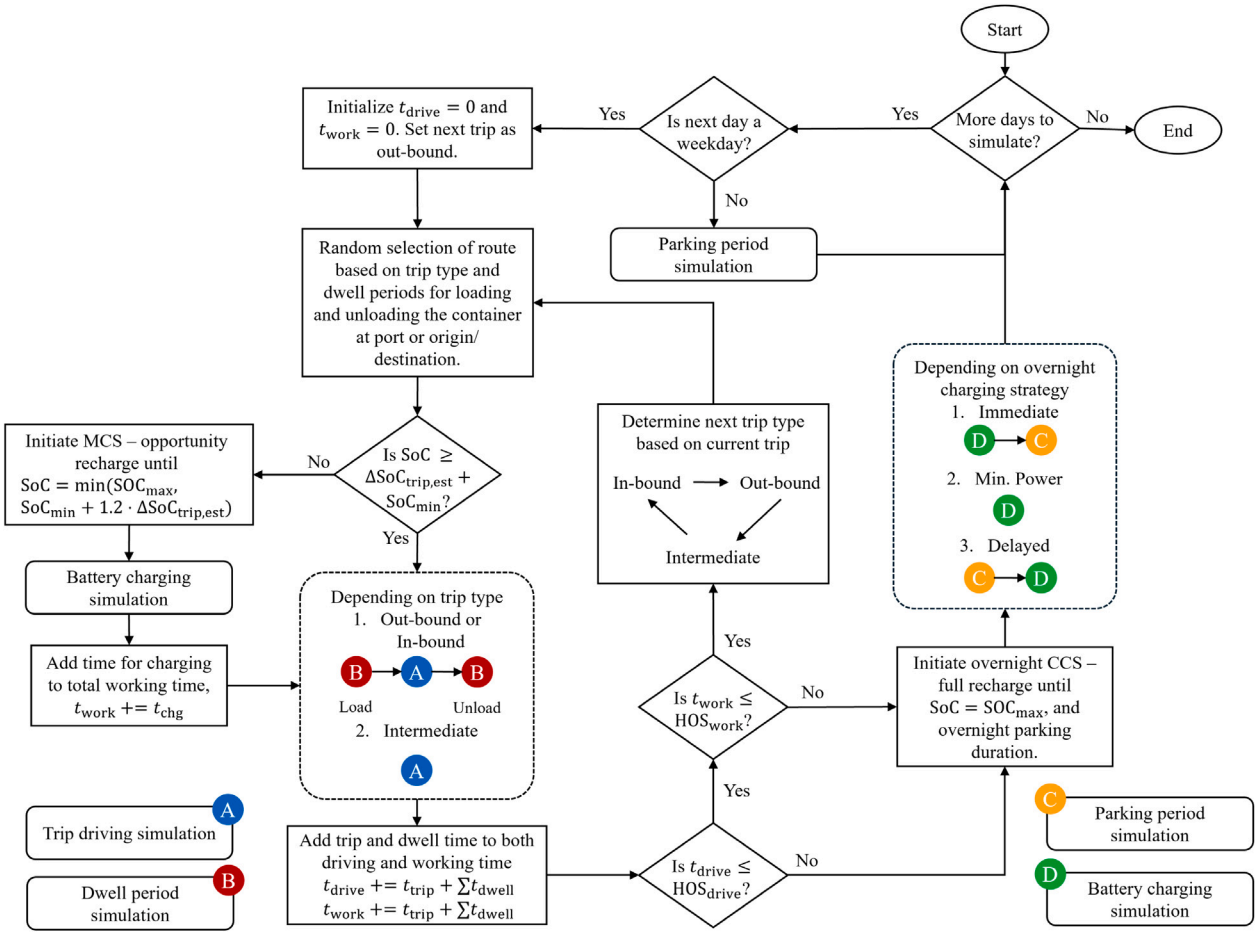

Fig. 5. Algorithm flow chart for simulating battery electric drayage truck daily operations.

and therefore, can be charged during the night without causing any potential scheduling conflicts. However, the three overnight charging strategies described above implicitly assume a one-to-one relationship between chargers and electric trucks, driven by the extended plug-in durations required for delayed and minimum-power overnight charging. Under the delayed charging strategy, vehicles remain connected for long periods but are not actively charged until later in the night so that charging concludes just prior to the next day's operations. Similarly, the minimum-power strategy requires vehicles to remain connected overnight or for extended durations during weekends. Under conventional charging architectures, these requirements can drive higher upfront infrastructure investments for fleet operators. Alternative architectures that decouple physical vehicle connections from dedicated chargers – potentially incorporating dynamic power allocation and vehicle queuing – could substantially reduce charger requirements and overall capital costs. Such approaches are not evaluated in this study and are identified as an important area for future work.

In addition to overnight charging, battery electric trucks can also perform opportunity charging at ports or various origin/destination (O/D) locations using Megawatt Charging Systems (MCS) chargers. In this study, the maximum charging power of MCS chargers is limited to 440 kW. Opportunity charging is designed not to charge the battery fully but to provide enough charge for the truck to complete its next trip. The opportunity charging can only be performed prior to the start of the trip, and no charging can take place at an intermediate stop such as at a charging station on the route. This condition restricts the number of routes that can be serviced by BETs with smaller battery packs.

Fig. 5 shows the algorithm designed to emulate the drayage truck operation in the virtual simulations. The algorithm is implemented in MATLAB, and simulations for driving, charging, and stationary periods are performed using the Simulink models. In the algorithm, the description of the variables is as follows: t_{drive} is the total driving time for a day, t_{work} is the total working time for a day, t_{chg} is the charging time, and $\sum t_{dwell}$ is the total dwell period that includes the container loading and unloading times sampled from their probability distributions depending on the type of trip (out-bound or in-bound), and t_{trip} is the trip driving time. $\Delta SoC_{trip,est}$ is the estimated SoC depletion of the trip based on route, ambient temperature and air density, and vehicle weight. SoC_{min} and SoC_{max} are the minimum and maximum allowed SoC for the battery, respectively. For both driving and working, the HOS limits are given by HOS_{drive} and HOS_{work}, respectively.

3. Results and discussion

3.1. Cycling aging model calibration

In order to estimate the BETs lifetimes under usage, the proposed empirical degradation models are first calibrated to experimental data.

For cycling-based aging, an expansive open-source data set collected from a set of aging campaigns performed at Sandia National Laboratory and reported in [54] is used for calibration purposes. Specifically, the 100% depth-of-discharge subset from [54] is used in this work, in which commercial NMC and LFP cells were cycled under constant-current square-wave protocols at C-rates between 0.5 C and 3 C and held at fixed chamber temperatures of 15 °C, 25 °C, and 35 °C. This subset was selected as it represents the most conservative branch of the dataset, providing an upper-bound estimate on cycling-induced

Table 2
Cycle aging model parameters for NMC and LFP obtained from calibration.

Chemistry	a_{cyc} (%/[K^2 · Ah$^{\zeta_{cyc}}$])	b_{cyc} (%/[K · Ah$^{\zeta_{cyc}}$])	c_{cyc} (%/Ah$^{\zeta_{cyc}}$)	d_{cyc} (K)	e_{cyc} (h · K)	ζ_{cyc} (–)
NMC	$8.581 \cdot 10^{-7}$	$-5.182 \cdot 10^{-4}$	$7.867 \cdot 10^{-2}$	$1.797 \cdot 10^{3}$	$-2.997 \cdot 10^{1}$	0.6
LFP	$6.693 \cdot 10^{-6}$	$-3.875 \cdot 10^{-3}$	$5.620 \cdot 10^{-1}$	$5.287 \cdot 10^{1}$	$9.084 \cdot 10^{1}$	0.9

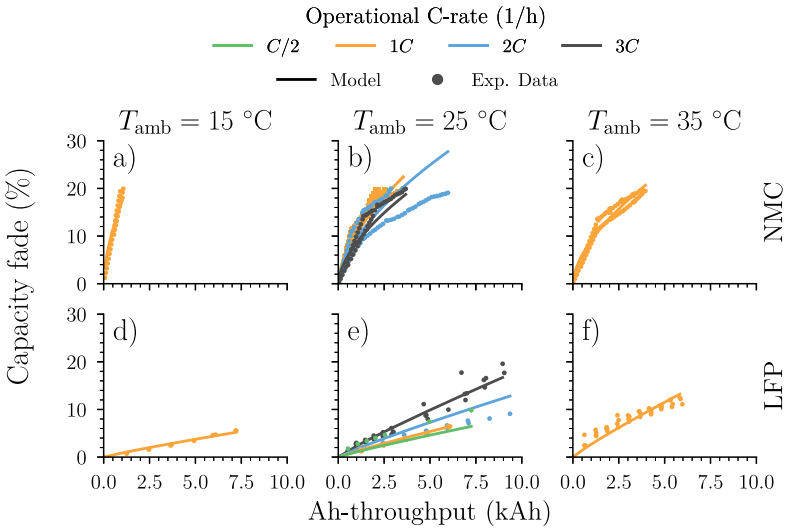

Fig. 6. Cycling aging model data (dots) and calibrated model prediction (lines) comparisons for (a–c) NMC and (d–f) LFP battery cell chemistries. Each columns of plots: different ambient temperatures, increasing left-to-right. Colors: different operational C-rates. Detailed breakdown of error metrics for the different conditions can be found in Appendix A.4.

degradation. These calibrated stressor dependencies are then applied to realistic heavy-duty drayage duty cycles in the fleet simulation.

Following the procedure described in Section 2.2.5, in Step 3 the following form of the severity factor function to characterize cycling-based aging for both the battery chemistries is proposed in this work:

$$\sigma_{cyc}^{model}(T_{cell}, I_C; \theta_{cyc}) = \left| a_{cyc} T_{cell}^2 + b_{cyc} T_{cell} + c_{cyc} \right| \cdot \exp\left(\frac{d_{cyc} + e_{cyc} \cdot |I_C|}{T_{cell}} \right) \tag{44}$$

The cell temperature polynomial in the absolute value, alongside the Arrhenius-like term, imposes that there is a range of temperatures at which cycling aging is relatively low and otherwise is higher outside of this preferred range. This enforces the known phenomenon that battery operation in cold or hot conditions accelerates battery degradation relative to use in moderate temperature conditions [55,56]. The absolute value is applied to the cell temperature polynomial to ensure that the predicted degradation is always positive. The presence of the operational C-rate, I_C in the exponential enforces the expectation that higher operational C-rates lead to a higher expected cycling degradation [57]. The cycling-based aging severity factor function is thus characterized by five parameters, $\theta_{cyc} = \begin{bmatrix} a_{cyc} & b_{cyc} & c_{cyc} & d_{cyc} & e_{cyc} \end{bmatrix}^T \in \mathbb{R}^5$. The parameter values and the optimal value of the exponent obtained from the calibration procedure are summarized in Table 2 for both battery cell chemistries considered.

Comparing the predictions of the calibrated cycle aging model for both cell chemistries to the experimentally collected data [54], a good agreement between the model predictions and the experimental data is observed as seen in Fig. 6 with an average root-mean-square error (RMSE) of ≈ 2.1% for NMC and ≈ 1.17% for LFP.

The calibrated cycle-aging empirical model for NMC cells predicts an unexpectedly low cycle life, with the battery expected to reach end-of-life – defined here to be 20% capacity fade – within approximately 300 equivalent full cycles. This is a feature of the data and can be seen in Fig. 6b. This prediction deviates significantly from manufacturer claims for NMC cells, which typically average around 2000 cycles, as determined from the dataset provided in [58]. To address this discrepancy, the severity factor function is modified, decreasing its magnitude by a factor ≈ 3.81, to align with the manufacturer-reported cycle life for a standard case of a 1C charge–discharge cycle at a fixed ambient temperature of T_{amb} = 25 °C. The modified values for the NMC cycle-aging model are listed in Table 3. This adjustment ensures the model reflects more realistic cycle-life expectations for NMC cells, enabling more accurate assessments of long-term battery performance under typical operating conditions.

In contrast, the calibrated cycle-aging model for LFP cells predicts that battery end-of-life is reached in approximately 4100 equivalent full-cycles which falls within the expected range of cycle-life for this chemistry from manufacturer reports [58]. As such, the LFP cycle-aging model parameters were not modified and implemented as reported in Table 2.

3.2. Calendar aging model calibration

Calendar aging is proposed to be characterized by a severity factor function of the form:

$$\sigma_{cal}^{model}(T_{cell}, SoC_{store}; \theta_{cal}) = k_{ref} \cdot \left| a_{cal} \cdot (SoC_{store} - b_{cal})^{p_{cal}} + c_{cal} \right| \cdot \exp\left[-\frac{E_A}{R} \left(\frac{1}{T_{cell}} - \frac{1}{T_{ref}} \right) \right] \tag{45}$$

Here, R = 8.3145 J/mol K denotes the universal gas constant. The p_{cal}th-order polynomial in storage SoC ensures that the severity factor function increases when the battery is stored at higher SoCs. Similarly, the Arrhenius term is introduced to ensure that higher storage temperatures result in a larger degree of aging. The absolute value around the storage SoC polynomial, similar to the severity factor function for cycling aging, is placed to enforce that capacity loss is always positive. The severity factor function for calendar aging is parameterized with five parameters, $\theta_{cal} = \begin{bmatrix} k_{ref} & a_{cal} & b_{cal} & c_{cal} & E_A \end{bmatrix}^T \in \mathbb{R}^5$, and

Table 3
Modified cycle aging model parameters for NMC that aligns with manufacturer claims.

Chemistry	a_{cyc} (%/[K^2 · Ah$^{\zeta_{cyc}}$])	b_{cyc} (%/[K · Ah$^{\zeta_{cyc}}$])	c_{cyc} (%/Ah$^{\zeta_{cyc}}$)	d_{cyc} (K)	e_{cyc} (h · K)	ζ_{cyc} (–)
NMC	$2.254 \cdot 10^{-7}$	$-1.360 \cdot 10^{-4}$	$2.064 \cdot 10^{-2}$	$1.797 \cdot 10^{3}$	$-2.997 \cdot 10^{1}$	0.6

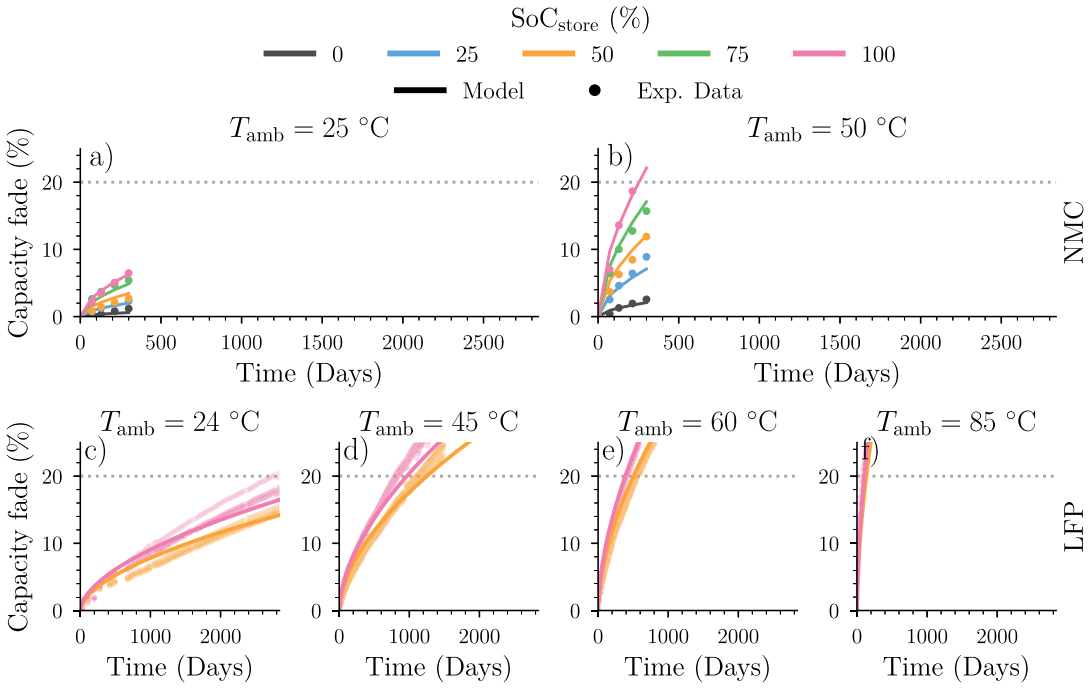

Fig. 7. Calendar aging model experimental data (points) and calibrated calendar aging model predictions (lines) for (a–b) NMC111 and (c–f) LFP battery cell chemistries. Different plots correspond to different ambient temperature conditions. Different colors in a plot: storage SoCs. NMC111 experimental calendar aging data is obtained by digitizing [7]. LFP data is obtained from [59]. The temperature and SoC ranges shown reflect the experimental conditions and are retained here without rescaling to preserve the original source measurements. A detailed breakdown of error metrics for the different conditions can be found in Appendix A.4..

Table 4
Calendar aging model parameters for both battery cell chemistries.

Chemistry	k_{ref} (%)	a_{cal} (%)	b_{cal} (%)	p_{cal}	E_A (J/mol)	ζ_{cal} (–)
NMC	$1.68 \cdot 10^{2}$	$1.262 \cdot 10^{-5}$	$1.314 \cdot 10^{-6}$	1	$3.949 \cdot 10^{4}$	0.577
LFP	$2.479 \cdot 10^{1}$	$2.245 \cdot 10^{-3}$	$1.927 \cdot 10^{-2}$	3	$3.144 \cdot 10^{4}$	0.572

these values are calibrated for the LFP battery chemistry based on data from [59]. Due to data limitations in [59] for the NMC battery chemistry, only the time exponent value is derived from this dataset. To obtain the severity factor function model parameters for the NMC battery chemistry, data digitized from [7] is used instead. The calendar aging model parameter values obtained after calibration are reported in Table 4.

Comparing the calibrated calendar aging model predictions to the experimentally collected data in Fig. 7, it is found that the average error between the model and the experimental data, where the average is over all of the stress factors and storage times, is less than 1% for the NMC and is less than 2% for LFP (see Appendix A.4 for a detailed breakdown of error metrics as a function of storage conditions). As such, we conclude that the models obtain good agreement with the data. The calendar aging response curves shown in Fig. 7 are meant to demonstrate that the proposed semi-empirical framework successfully reproduces the experimentally observed sensitivity trends for each chemistry under its respective stressor conditions. The publicly available datasets on which these surfaces are based were generated using different temperature and SoC ranges, and the original ordinate scales are retained to preserve fidelity to the source measurements. Notably however, the span of these experimental conditions covers the operating envelope experienced by the simulated battery pack in our ABM. Accordingly, the calendar aging model is applied strictly in an interpolative regime, avoiding extrapolation into temperature and SoC domains not represented in the calibration data.

3.3. Simulated drayage truck activity at Port of Savannah, GA

This section presents the activity generated for diesel trucks and BETs operating in the drayage application at the Port of Savannah, GA. For each combination of battery size, chemistry, and overnight charging strategy, 10 trucks per case are simulated using the ABM algorithm presented in Section 2.4. To induce variability, half of the simulated trucks in each case start their service at the beginning of a year, while the other half begin their service at the middle of the year. Diesel drayage trucks serve as a baseline to ascertain whether simulated drayage operations mirror actual conditions. Fig. 8 depicts the serviceable route locations based on the different types of trucks. Increasing the battery size of the BETs allows for more route coverage from/to the port. BET driving range increases from 180 to 260 miles as the battery size is doubled from 400 to 800 kWh. In addition, it is evident from the comparison of the number of points within the maximum range of the 800 kWh battery pack vehicles compared to the diesel case in Fig. 8, that the BET with an 800 kWh battery pack is capable of covering almost all routes compared to the diesel truck. Furthermore, Fig. 9 shows boxplots of the completed trip distance in different capacity fade bins for various battery sizes. As the battery capacity fades, the BETs are not able to cover the trips that were possible when the battery was relatively new (0%–4% capacity fade). In the case of BETs with 400 kWh battery packs, the maximum trip distance

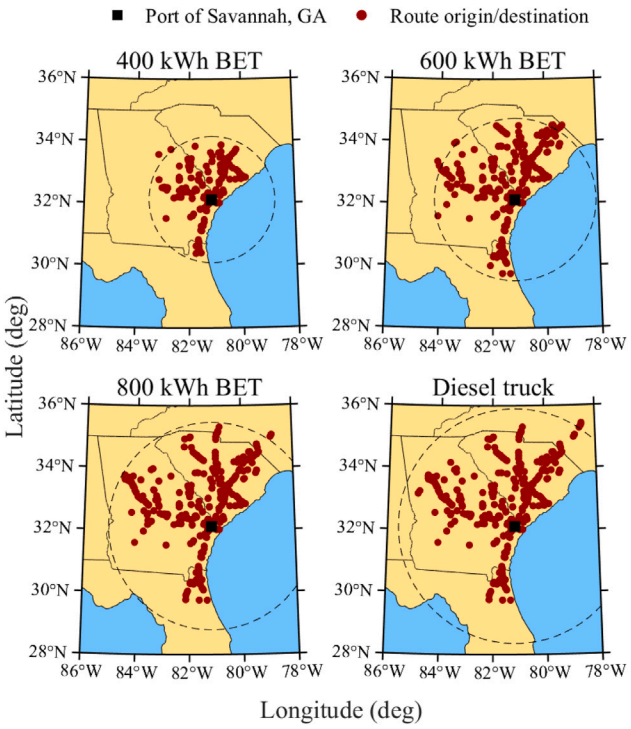

Fig. 8. Drayage routes coverage by simulated BETs and diesel trucks operating at Port of Savannah, GA.

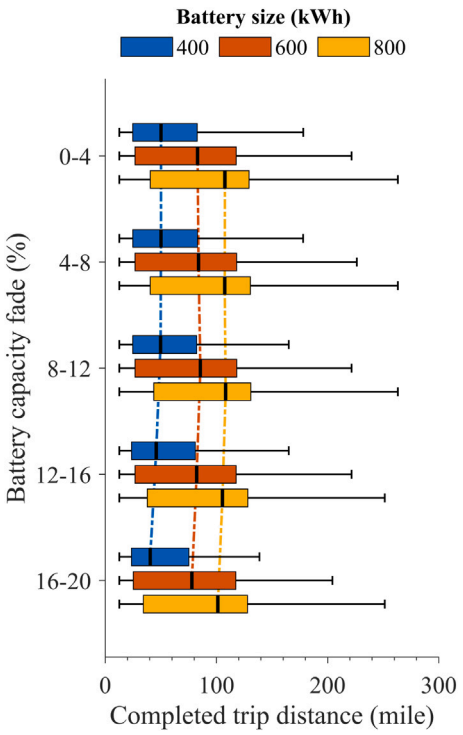

Fig. 9. Reduction in the accessible trips with reduction in battery capacity as the battery degrades.

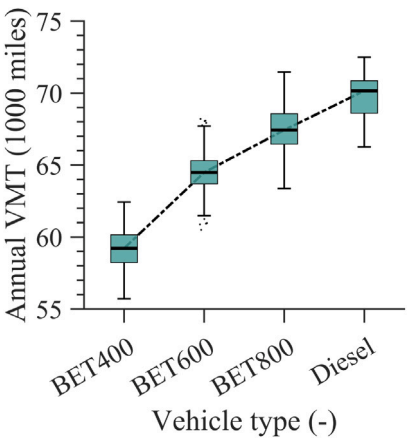

Fig. 10. Annual VMT of the simulated BETs and diesel truck in drayage application.

reduces from 180 mile to 140 mile, as battery degrades. The reduction in accessible trips is less pronounced in the case of larger sized battery packs which only observe a reduction in maximum trip distance of 20 miles. Importantly, the resulting simulated fleet energy consumption (~2.2 kWh/mile) aligns with the bulk energy use estimates reported by NACFE for early electric freight deployments [60], supporting the representativeness of the applied operational profiles within available data constraints.

Due to the differences in the route coverage by the different vehicle types (Diesel and BETs), there are significant differences in terms of the annual vehicle miles traveled (VMT) and the count of daily trips. BETs with smaller battery sizes can only cover shorter routes compared to their larger counterparts, which, when accumulated over a year, results in a reduced annual VMT for BETs with smaller battery packs compared to those with larger batteries, as seen in Fig. 10. Deliveries on shorter routes can be completed faster compared to longer routes and enable more frequent daily visits of smaller battery pack BETs to the port, as seen in Fig. 11. The 400 kWh battery pack size BETs can perform up to 6 daily trips in this idealized drayage scenario, whereas, increasing battery size leads to a reduction in the number of daily trips. Finally, the weight distribution of the simulated drayage trucks is shown in Fig. 12. BETs are substantially heavier than diesel trucks. Enlarging the battery size results in a more rightward shift in the weight distribution histograms. Diesel truck weights are capped at an 80,000 lbs gross combined weight rating (GCWR), whereas electric trucks have a 2000 lbs allowance for a maximum of 82,000 lbs. Since identical cargo-weight distributions are used in all the simulations, the overall weight of a BET could exceed the GCWR; however, in such simulations, the BET's weight is restricted to the Class-8 GCWR for electric trucks, with anything over that being counted as lost payload.

The charging model (42) is calibrated using reported data from a Tesla Model S Plaid from [61]. The rated power SoC window used in the model spans from $SoC^{min}_{max\ win} = 10.5\%$ to $SoC^{max}_{max\ win} = 65\%$ with an exponential coefficient of $B = 0.3$. These parameters are held constant across different rated charger powers $P_{charger,rated}$. The left-hand plot of Fig. 13 shows the resulting charging curve for the CCS and MCS chargers considered in this study.

The daily operations model, in conjunction with the charging model, allows for exploring the distinct charging behaviors for the fleet based on battery size and charging event type, as shown in the Sankey diagrams in Fig. 13. All trucks are designed to reach 95% by the end of the night during overnight charging, regardless of the charging strategy used. Most overnight charging sessions begin with batteries in a relatively low SoC range (15%–35%), with this particularly being a prominent state for smaller batteries, suggesting that vehicle batteries are largely depleted by the end of the operational day. In contrast, opportunity charging has a much wider distribution of SoC levels at the start and end of the charging event. These distributions reflect the variable and time-constrained nature of opportunity charging, where vehicles will only top-up to needed levels rather than charging to

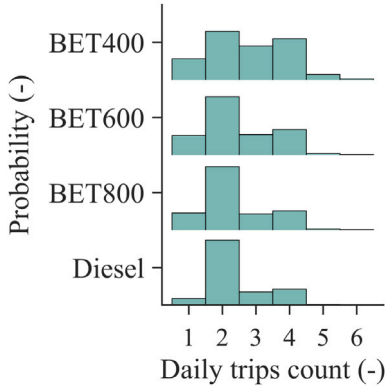

Fig. 11. Daily trip counts for the simulated drayage trucks. Each time a truck visits the port, whether to drop off a container or to pick one up, it is recorded as an individual trip.

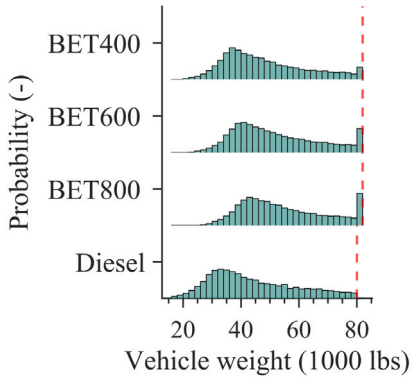

Fig. 12. Vehicle weight distribution of simulated BET and diesel drayage trucks. The red dashed line represents the GCWR of Class 8 trucks depending on powertrain type.

full every time. As the battery size increases, the variability becomes even more pronounced, with larger batteries (e.g., 800 kWh) showing greater flexibility in charging behavior and less reliance on reaching a full charge after opportunity charging. Meanwhile, trucks with smaller batteries depend more heavily on maximizing their SoC during each charging session.

3.4. Battery degradation trajectories obtained using daily drayage operation

The reduction in battery capacity resulting from the drayage activities of the BETs at the Port of Savannah, GA, is evaluated over a 10-year service period for each truck. As previously discussed, 20% capacity fade of the battery pack is defined as the end of the battery system's useful life in this work. At that point, the BET battery pack is replaced with a new battery pack of identical size and chemistry to the original. Fig. 14 shows the battery capacity degradation trajectories observed in the initially installed battery packs in BETs, considering various combinations of battery chemistry, size, and overnight full charging approaches.

Variations in battery degradation trajectories can be attributed to the battery chemistry, the size of the battery, and the strategy employed for overnight full charging. When comparing batteries of identical size and using the same overnight full charging strategy in Fig. 14, the LFP battery system is observed to offer a longer service life when compared to the NMC battery system. This result is consistent with the empirical observation that LFP cells generally exhibit a longer lifespan (in the number of cycles) than NMC cells [58]. Moreover, while enlarging the battery size extends its lifespan, it is important to note that simply doubling the battery's size does not necessarily imply that its useful life will also be twice as long. Importantly, this is in stark contrast to the projections often made by rudimentary charge or energy throughput-based models [62]. Enhancing battery capacity by incorporating additional cells in parallel diminishes the current that each cell in the battery pack undergoes, leading to reduced current throughput for each cell. This, along with decreased stress levels due to a lower C-rate, contributes to less cyclic capacity fade. In contrast, the degree of calendar-aging based capacity fade is unaffected as it is not explicitly dependent on the size of the battery pack.

To further assess the influence of seasonal ambient conditions on the battery aging, the relative contribution of driving/resting activities in different seasons is shown in Fig. 15. Evidently there are different trends observed depending on the choice of battery chemistry. For the case of LFP, the summer months (June to August), which exhibit the highest ambient temperatures in Savannah, GA, are of major interest to the cumulative battery degradation over the full simulation horizon. Across the simulated configurations, ~27% of the total degradation was attributable to these months followed closely by the spring months (March to May), indicating that elevated ambient temperatures lead to a measurable but limited increment in lifetime fade. For the case of NMC battery packs, the colder seasons (winter and spring months) have slightly higher contribution to battery aging than the warmer seasons (summer and autumn). This modest seasonal influence is consistent with the battery thermal behavior observed in the simulations: (1) weekday rest periods are not of sufficient duration for the battery pack to thermally equilibrate with any high ambient temperatures encountered, due to the thermal inertia of the pack housing and cells, and (2) during daytime operation, the BTMS actively regulates the pack temperature toward its acceptable operating band. Consequently, significant excursions into temperature regimes associated with accelerated calendar aging occur primarily during extended weekend rest periods rather than during daily operational cycles. This suggests that, under realistic thermal management and operational scheduling for heavy-duty electric trucks, ambient seasonal temperature variation in this region contributes to degradation in a bounded manner rather than being a dominant driver of lifetime fade.

Note that alternative architectures such as battery swapping, recently reconsidered for heavy-duty fleets due to the high cost fraction of the pack relative to vehicle value, could further decouple vehicle utilization from charging dwell time [63–65]; however, such logistics-dependent architectures introduce additional operational degrees of freedom (e.g., pack circulation, swap station scheduling) and are therefore considered outside the scope of the present plug-in charging framework [63,66].

The simulation framework presented in this study also allows evaluation of the influence of various overnight full-charging strategies on the battery pack's capacity fades. As seen in Figs. 16 and 17, although the charging time results in the same Ah-throughput between the delayed and immediate overnight charging strategies thereby resulting in identical levels of cycle-based aging, there remains a significant difference in the degree of calendar aging, due primarily to the differences in the storage SoC that the battery pack experiences under these two strategies. In particular, the share of capacity fade for parking-weekday and parking-weekend activities is significantly reduced in the delayed strategy compared to the immediate strategy, although the fraction of time spent in the parking mode is the same. Under the min. power strategy, the amount of time spent where the battery is not being used is reduced to an insignificant amount and instead, the fraction of time associated with the overnight strategy becomes the highest of any of the activities. Accordingly, the amount of capacity fade associated with parking activities where the battery is not being used also drops to insignificant levels.

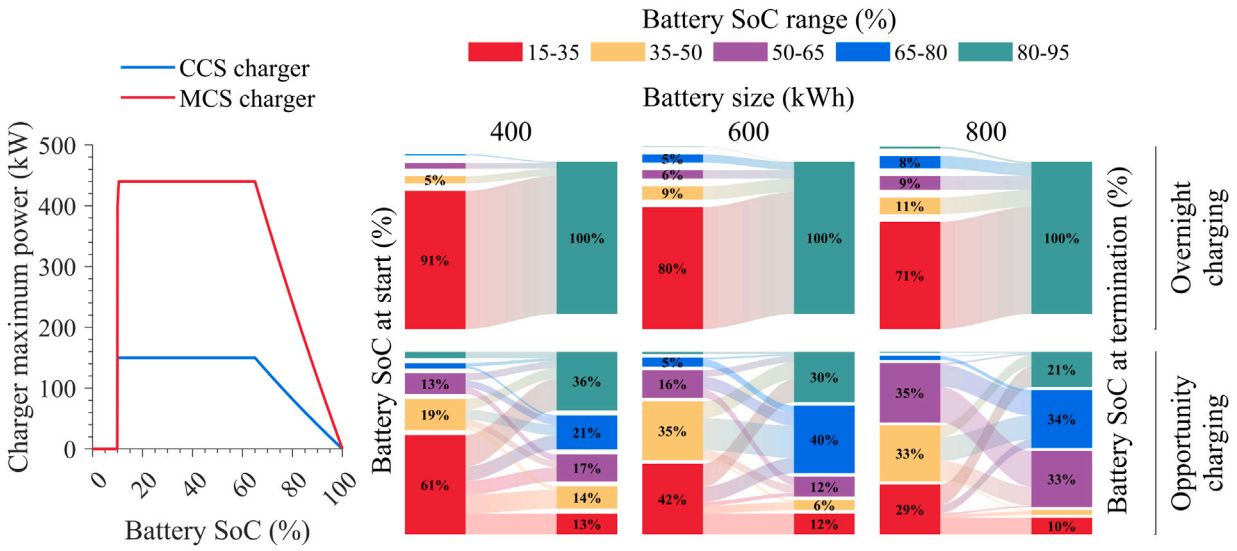

Fig. 13. On left, the maximum power profiles for 150 kW CCS and 440 kW MCS chargers used in overnight and opportunity charging, respectively. The Sankey diagram on the right shows the flow of the starting (left axis) and termination (right axis) battery SoC (%) of simulated charging events. Each side represents the share of charging events starting or ending within a specific SoC range, adding up to 100%. The width of lines is proportional to the number of overnight and opportunity charging events.

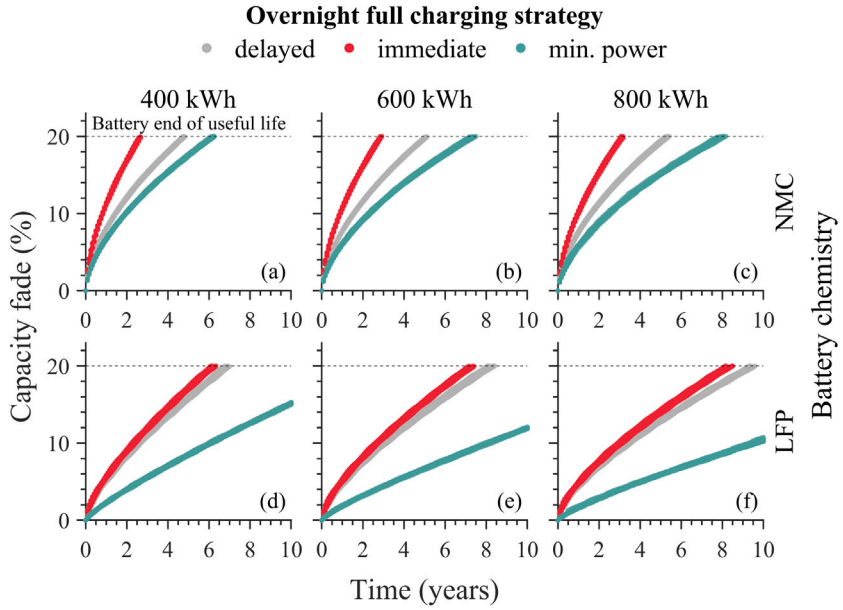

Fig. 14. Battery degradation trajectories resulting from use of BETs in simulated drayage application at the Port of Savannah, GA. Columns represent different battery sizes, while rows represent the battery chemistry (NMC: a, b, and c, while LFP: d, e, and f). Different colors in the subplots are for the employed overnight full charging strategy for the BETs.

Interestingly, the choice of overnight charging strategy leads to significant differences in the lifespan of NMC battery systems, with the immediate and minimum power strategies attaining the lowest and highest system lifetimes, respectively. In contrast, the system lifetime observed from the immediate and delayed overnight charging strategies is notably similar for LFP battery packs, while the minimum power overnight charging strategy resulting in a battery system lifetime exceeding the BETs service life. In general, the findings inform that the immediate charging strategy leads to the highest rate of battery capacity fade for both chemistries. These results suggest that the use of an immediate overnight charging strategy would result in significantly reduced lifetimes for the vehicle's battery system while the minimum power charging strategy accrues the greatest benefit in extending the battery system lifetime.

In addition, the sensitivity associated with each activity can be computed as the ratio of the total amount of capacity fade caused by a given activity to the amount of time spent performing that activity. This is shown in the bottom set of plots in Figs. 16 and 17. Strikingly, the greatest sensitivity is observed to be associated with opportunity (or fast) charging during the day. This indicates that a disproportionately large amount of the battery pack degradation still occurs due to the high rates of current that is experienced, despite opportunity

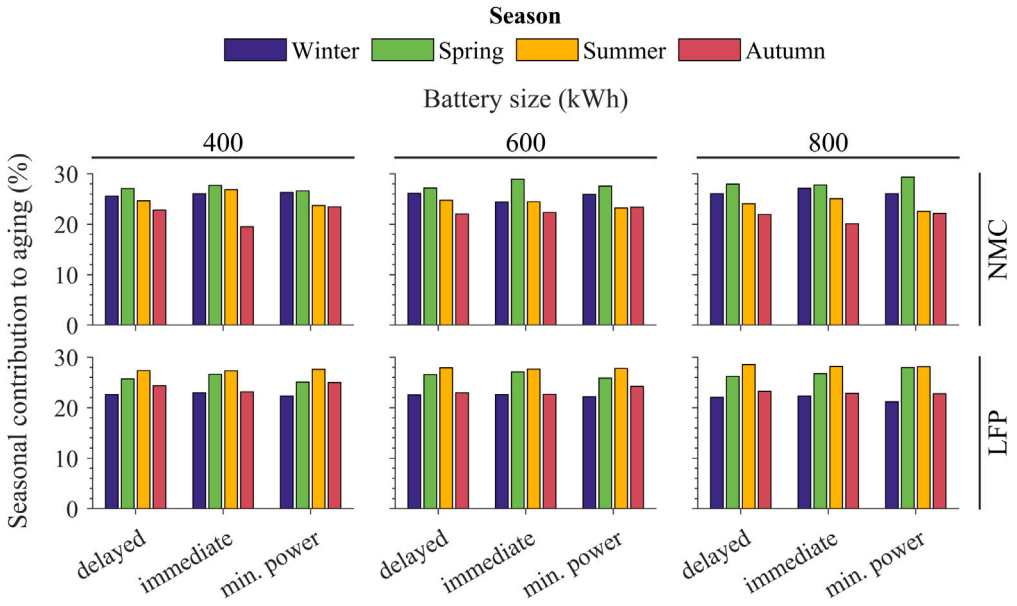

Fig. 15. Seasonal contribution to battery aging. Seasonal contribution is determined by dividing the amount of battery capacity loss in a given season by the total battery capacity loss. The columns represent the different battery sizes, while the two rows represent the different battery chemistry.

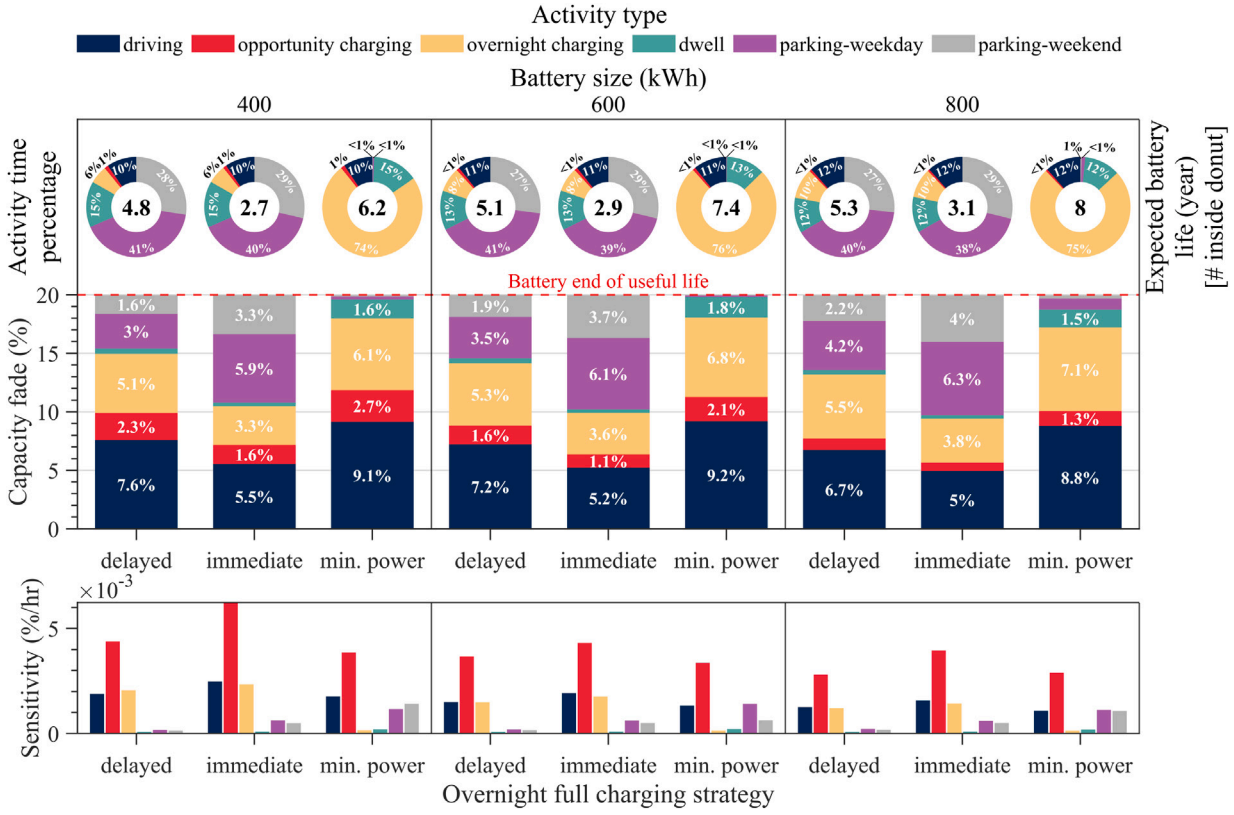

Fig. 16. Contribution of different vehicle activities to battery aging of NMC battery packs and their sensitivity to battery degradation. Top subplots: the donut plot shows the percentage of time spent performing each activity. The number in the center of the donut is the battery life (years) for the choice of battery size and overnight full charging strategy. Middle subplots: the stacked bar plot represents the average capacity fade caused by each activity over the lifetime of the battery operations. Bottom subplots: the grouped bar plots show the aging sensitivity of different vehicle activities. The sensitivity is measured as the amount of capacity fade in % for every hour of the vehicle activity. Different colors represent different vehicle activities.

charging only taking up a very small fraction of the overall time in the BET's service life. Furthermore, as the battery size is increased for each chemistry it is observed that the sensitivity decreases for driving and charging activities. As discussed previously, a larger battery size corresponds to a higher capacity system with more battery cells placed in parallel, thus resulting in a lower C-rate experienced by each cell, thereby resulting in a lower cycling aging. For a given battery size, comparing the aging sensitivity of the parking-based activities, as the

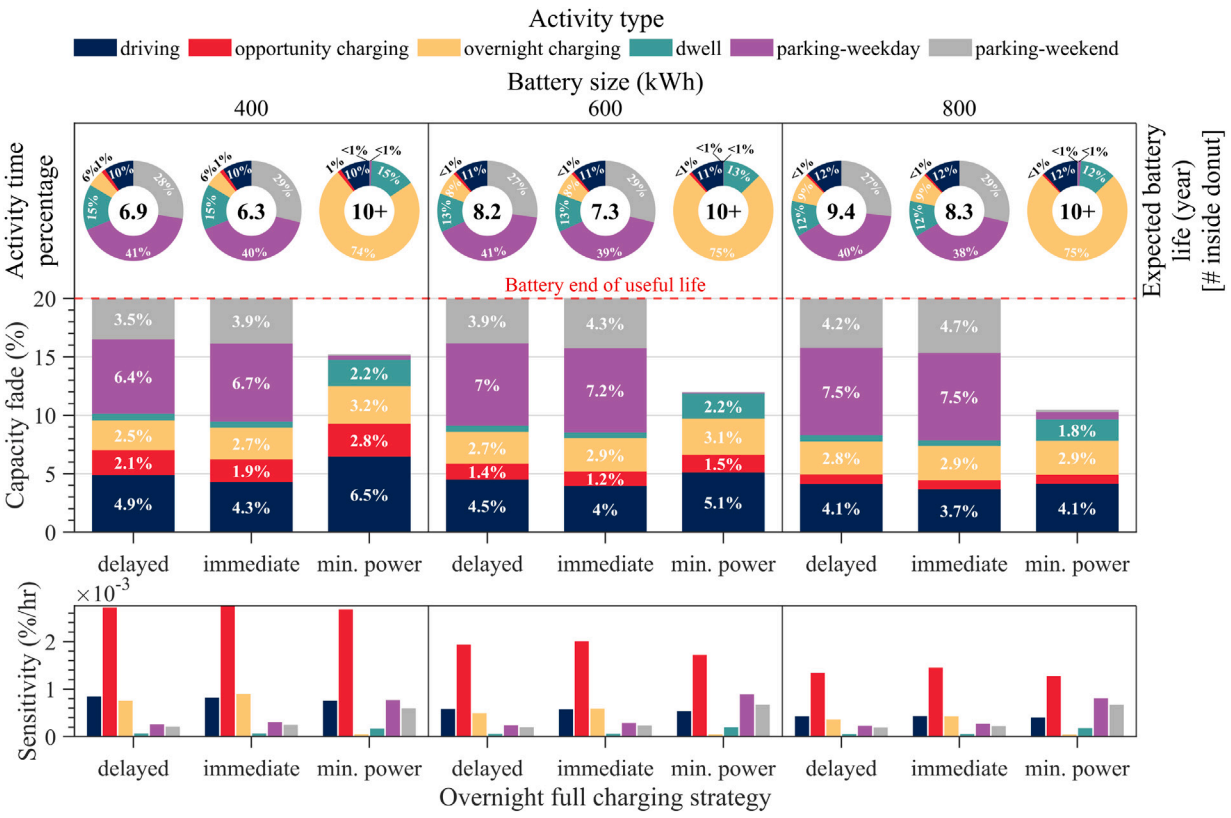

Fig. 17. Contribution of different vehicle activities to battery aging of LFP battery packs and their sensitivity to battery aging. Same colors and styles as Fig. 16.

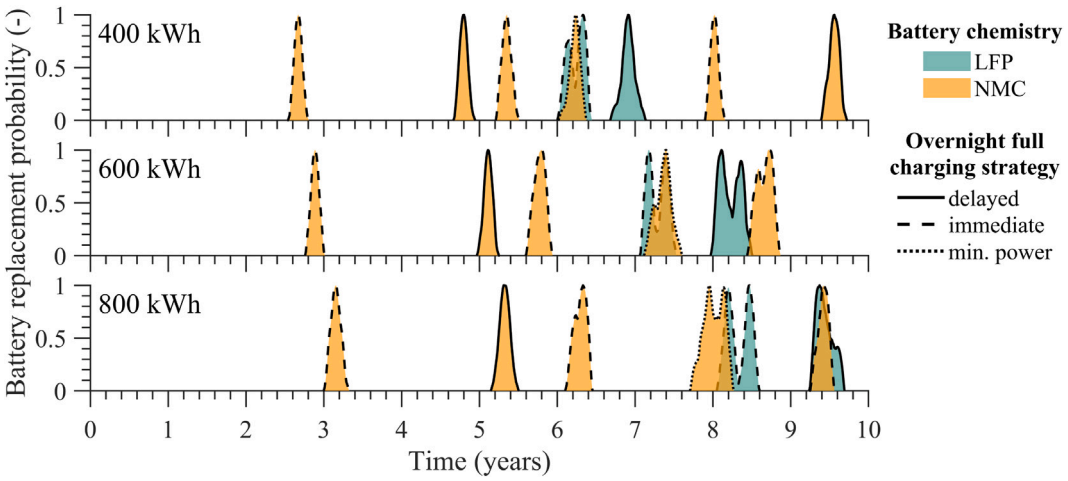

Fig. 18. Battery replacement period for drayage BETs.

overnight full charging strategy is changed from immediate to delayed, it is seen that the sensitivities decrease, consistent with these activities causing less capacity fade for the same fraction of time between the two strategies.

Additionally, by analyzing the simulation results for BETs with the same battery size, chemistry, and overnight charging strategy the statistics on battery replacement periods are also determined and are shown in Fig. 18. Depending on the choice of battery and overnight charging strategy for BETs, the battery may need replacement to complete the truck's intended 10 years of service, as set in this case study. It is found that smaller battery packs require more frequent replacements compared to larger-sized packs. Battery packs of NMC chemistry for all pack sizes require three battery replacements (the first replacement around 2.5–3.5 years, the second between 5.5–6.5 years, and the third between 8–9.5 years depending on battery size) when employing the immediate overnight charging strategy. This high number of battery replacements is due to the accelerated calendar aging that takes place due to high storage SoC as a consequence of immediately fully charging the battery pack after every shift end. For the delayed overnight charging strategy, a BET with a 400 kWh battery pack requires two battery replacements (the first at around 5 years and the second at the 9.5-year mark). The remaining combinations of battery sizes and overnight charging strategies require at least one battery replacement to complete the 10 years of truck service. In comparison, only one battery replacement is required for all the BETs with LFP battery chemistry employing a delayed and immediate overnight charging strategy,

with the replacement taking place later in time for BETs using the delayed charging strategy. Notably, the originally installed 800-kWh LFP battery pack is predicted by the proposed simulation framework to last the entire 10 years of the truck's service life. Finally, minimum power charging proves to be the most favorable scenario for LFP battery packs, as it eliminates the need for any battery replacements in 10 years of service for all three battery sizes considered in this analysis, this however is not the true in case of NMC battery packs.

Although the above analysis was conducted to analyze the battery replacement considering 10 years of the truck's intended service in the drayage application with around 60,000–70,000 annual vehicle miles traveled, these results are equally applicable for evaluating cases with shorter service life requirements. Furthermore, fleet operators can use this kind of analysis, in conjunction with total cost of ownership tools, to determine the optimal battery and charging strategy according to their fleet operational requirements. Using this simulation analysis, the expected battery life depending on the choice of battery size and chemistry, along with the operation strategies, can be estimated. This battery life information can then be used to calculate the battery replacement timelines as well as the cost associated with replacing the battery pack. This particular study does not delve into such a techno-economic analysis. Still, interested readers are encouraged to consult Sujan et al. [67], which takes insights on the expected life of Li-ion battery packs from this study to determine the total cost of ownership of HD battery electric drayage trucks at the Port of Savannah.

3.5. Boundary conditions and limitations

While this study provides system-level insights into the long-term degradation behavior of electrified heavy-duty drayage trucks, the modeling framework developed is intended to support comparative evaluation of battery chemistries, charging strategies, and operational practices, rather than to deliver absolute lifetime predictions for specific fleet deployments. Accordingly, the results should be interpreted within clearly defined boundary that reflect the scope of the case study, the availability of calibration data, and the modeling assumptions adopted. The following discussion explicitly summarizes these limitations and boundary conditions, while highlighting their implications for interpreting the present findings.

The conclusions drawn in this work are bounded by: operating temperatures (15 °C–45 °C), operating C-rates (up to 1.5 C), SoC operating ranges (10%–90%) represented in the experimental datasets used to calibrate the battery submodels, by battery chemistries (NMC and LFP), cell format (cylindrical), by the power demands estimated by the vehicle simulator that integrates information about the routes and temperature conditions in the Port of Savannah region, and by the assumption of effective thermal management and charge balancing allowing for the neglect of cell-to-cell variations within the battery pack system.

While the sub-component models of the vehicle simulator have been validated against controlled experimental datasets, large-scale operational degradation data from battery-electric Class-8 truck fleets are not yet publicly available, though pilot programs and early deployments have been initiated [68,69]. As such datasets become accessible, real-world drive cycle logs, BTMS thermal telemetry, and charging event histories may be used to validate the present simulation outputs and, where necessary, recalibrate specific subcomponents of the vehicle model to improve alignment with field-observed degradation trajectories. Additionally, having real-world battery degradation data can enable the development of data-driven algorithms for estimating the state-of-health of the battery pack from relevant features relating the daily vehicle operations to different battery degradation phenomena in Li-ion batteries [70,71].

The simulation framework relies on semi-empirical aging models calibrated to specific datasets, which does not explicitly resolve all underlying degradation mechanisms, particularly under extreme or highly variable operational conditions. The cycling aging models are calibrated using constant-current, full depth-of-discharge experiments; however, the degradation formulation is expressed as a function of cumulative Ah-throughput modulated by instantaneous stress factors, namely operational cell temperature and C-rate. This formulation enables the aggregation of arbitrary, time-varying current profiles without reliance on explicit cycle counting [72]. The use of full-depth, constant-current calibration data thus provides a conservative upper bound on per-Ah degradation severity, while dynamic operation is naturally captured through time-resolved stress factor evaluation. Nevertheless, cycle-history-dependent effects and nonlinear interactions between shallow and deep cycling are approximated and the creation and inclusion of more faithful representations of these effects constitute an important direction for future aging model refinement.

In practice, cell-to-cell variations in capacity, impedance, and thermal exposure can induce localized acceleration of degradation, with the earliest-failing cell defining the functional end-of-life of the pack. The present formulation does not explicitly capture such localized effects but instead evaluates the cumulative aging of an equivalent homogeneous cell subjected to the aggregate thermal and electrical load histories derived from the vehicle model. Although the use of experimentally calibrated aging models based on constant-current cycling data introduces a degree of conservatism [73], and active thermal management reduces macroscopic gradient formation, the omission of intra-pack heterogeneity means that the lifetimes reported here should be regarded as optimistic estimates achievable under well-regulated thermal and charge balancing control. Future work incorporating reduced-order heterogeneous pack models, weakest-cell propagation mechanisms, or a digital twin-based electrochemical modeling from the cell-to-pack scale could further resolve the influence of variance growth on pack retirement thresholds [74].

The operational scenarios considered in this study are idealized representations of drayage activity and may not capture the full range of real-world variability, including variable driver behavior [75], changing routes [76], or infrastructure constraints [67]. While such factors may influence absolute lifetime estimates, the relative sensitivity of degradation trends to charging power, resting SoC, and battery chemistry is expected to remain qualitatively robust across a broad class of drayage operations.

The computational cost associated with the high-fidelity, long-time-horizon simulations ultimately constrained the number of scenarios analyzed, limiting the exploration of more diverse operational conditions or alternative charging infrastructure setups. Future research should aim to refine the aging models to the specific cells that vehicle manufacturers today are using, streamline computational demands through reduced-order modeling, and expand the framework to include broader operational and economic considerations, such as vehicle-to-grid interactions and regional energy dynamics, thus leading to a more comprehensive analysis of electrified freight mobility and its associated infrastructure.

4. Conclusions

This study highlights the significant impact of daily operational practices on battery degradation in heavy-duty electric drayage trucks. By integrating advanced semi-empirical aging models, capturing both cycling and calendar aging, into a comprehensive vehicle simulation framework, the analysis revealed that LFP batteries outperform NMC batteries in terms of degradation resistance and service life due to their superior cycle durability. Larger battery packs showed reduced degradation rates owing to lower operational C-rates, but the relationship between size and lifespan was nonlinear, challenging basic throughput-based assumptions. Charging strategies emerged as a critical factor, with delayed and minimum power overnight charging significantly extending battery life compared to immediate charging, by reducing calendar aging effects from high resting states of charge. Additionally,

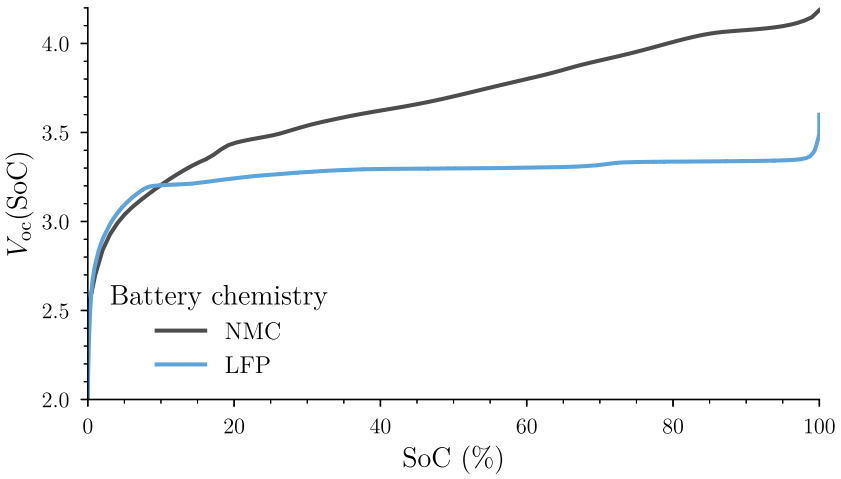

Fig. A.19. Open-circuit voltage curves for NMC (dark gray) and LFP (blue) battery cell chemistries.

high-power opportunity charging, despite its limited operational time, disproportionately contributed to aging due to elevated current stress. The charging scenarios explored in this work could, in the future, be extended and coupled with degradation-aware vehicle-to-grid (V2G) dispatch logic by using the capacity trajectory as a decision variable, although such system-level integration remains outside the scope of this study. These findings underscore the importance of tailored charging strategies and battery selection for specific fleet needs, while also advocating for infrastructure and policy support for lower-power charging and durable battery chemistries. This study provides actionable insights to enhance BET longevity, operational efficiency, and cost-effectiveness in electrified freight transportation.

CRediT authorship contribution statement

Ankur Shiledar: Writing – original draft, Visualization, Validation, Software, Methodology, Investigation, Formal analysis, Data curation, Conceptualization. **Joseph N.E. Lucero:** Writing – original draft, Visualization, Validation, Software, Methodology, Investigation, Formal analysis, Data curation. **Ruixiao Sun:** Writing – review & editing. **Manfredi Villani:** Writing – review & editing, Project administration. **Vivek A. Sujan:** Supervision, Project administration, Funding acquisition. **Simona Onori:** Supervision, Project administration. **Giorgio Rizzoni:** Supervision, Project administration.

Declaration of Generative AI and AI-assisted technologies in the writing process

During the preparation of this work, the author(s) used "Grammarly" and "ChatGPT" to improve wording, grammar, and punctuation. After using these tools/services, the author(s) reviewed and edited the content as needed and take(s) full responsibility for the content of the publication.

Declaration of competing interest

The authors declare that they have no known competing financial interests or personal relationships that could have appeared to influence the work reported in this paper.

Acknowledgments

This study received funding and support from the Department of Energy Vehicle Technologies Office, USA through the award WBS 7.2.0.502/FWP CEVT442, administered by the Oak Ridge National Laboratory's National Transportation Research Center.

Appendix. Battery model details

A.1. Battery model calibration

The same general procedure as described in [77] is followed to calibrate the coupled electrical and thermal models for the battery cell. Briefly, using experimental hybrid power pulse characterization data (HPPC) from [78] for NMC and [79] for LFP, the root-mean-square percentage error (RMSPE) is minimized,

$$\mathcal{O}_{\mathrm{RMSPE}}(\Theta) = 100\sqrt{\frac{1}{N_{\mathrm{meas}}}\sum_{n=1}^{N_{\mathrm{meas}}}\left(1-\frac{\mathcal{O}^{\mathrm{model}}(t_n;\Theta)}{\mathcal{O}^{\mathrm{data}}(t_n)}\right)^2} \tag{A.1}$$

between the experimentally measured signal $\mathcal{O}_r^{\mathrm{data}}$ and the model prediction $\mathcal{O}_r^{\mathrm{model}}$, where the index r distinguishes between voltage and temperature signals, by varying the parameters Θ of the model. Here, the Particle Swarm Optimization (PSO) algorithm is used to perform the parameter optimization [80]. To initialize the PSO, we follow the approach outlined by [35,77]. The initial ohmic resistance value R_0 is seeded from the high-frequency extracted from the HPPC pulse response and subsequently refined through transient voltage fitting. After refinement, R_0 should be interpreted as an effective lumped fast timescale resistance capturing both the true ohmic contribution and immediate polarization effects, rather than corresponding to a single frequency response. The relaxation timescale τ_1 is initially set equal to the pulse application duration, and the corresponding capacitance is estimated from the instantaneous voltage drop according to $C_1 = \tau_1(I_{\mathrm{cell}}/(V_1 - V_2))$, where V_1 and V_2 denote the voltage measured immediately after the pulse current application and just before pulse termination, respectively. Both τ_1 and C_1 are then refined by the PSO algorithm to best match the transient voltage trajectory.

A.2. Battery parameters

A representative cell of each chemistry is used to calibrate the models here. The NMC battery cell is represented by an LG Chem INR21700 M50T cell [81]. Electrical and thermal data for this cell under operation is published open-source in [78]. The representative cell for the LFP battery chemistry is a LithiumWerks ANR26650 M1B cell [82]. The electrical and thermal data for the LithiumWerks cell was collected in collaboration with an industry sponsor; however, it is not currently publicly available. The open-circuit voltage for both the representative cells are shown in Fig. A.19.

Following the calibration procedure described in Appendix A.1, for NMC, the ECM parameters as a function of SoC are obtained as shown

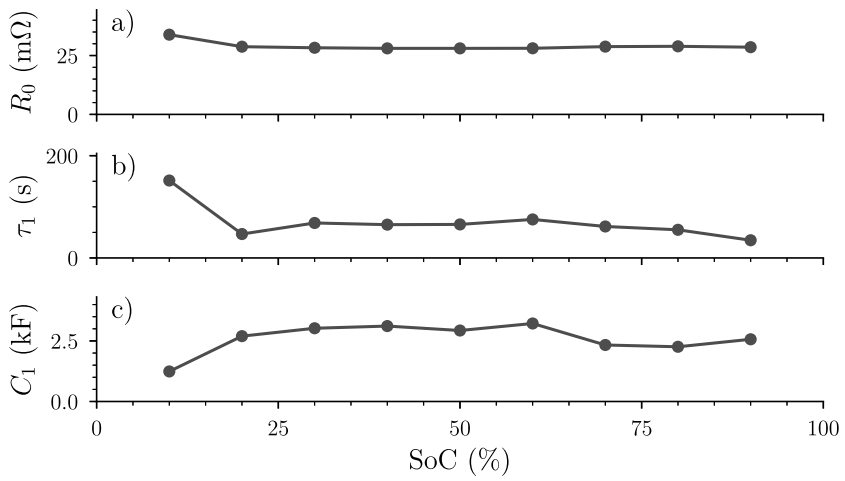

Fig. A.20. Equivalent-circuit model parameters as a function of SoC for NMC battery chemistry. (a) High-frequency resistance. (b) Polarization time scale. (c) Polarization capacitance.

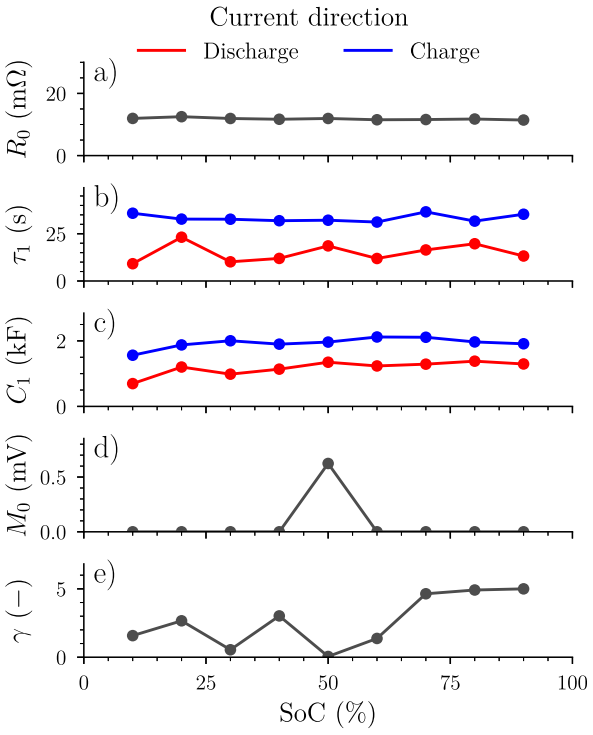

Fig. A.21. Equivalent-circuit model parameters as a function of SoC for LFP battery chemistry. (a) High-frequency resistance. (b) Polarization time scale. (c) Polarization capacitance. (d) Hysteresis voltage. (e) Hysteresis factor.

Table A.5
Table of thermal model parameters for both NMC and LFP chemistries.

Chemistry	C_{cell} (J/K)	$R_{\text{housing,cell}}$ (K/W)
NMC	158.625	2.664
LFP	2.739	0.823

in Fig. A.20. The corresponding set of parameters for the modified ECM used to describe LFP, as a function of SoC, is shown in Fig. A.21.

The thermal parameters obtained for each chemistry is summarized in Table A.5.

A.3. Battery model validation

To validate the calibrated models, a set of dynamic input current profiles is applied to both the model and experimentally to the respective cell in an open-loop fashion. Importantly, these profiles are distinct from the profiles used to calibrate the models. For the NMC cell, an input profile based on an Urban Dynamometer Driving Schedule (UDDS) [83] is used. In contrast, for the LFP cell and model, a hybrid HPPC and UDDS signal is used. The comparison between the model prediction and the collected experimental data is shown in Fig. A.22, where a good agreement between both NMC and LFP is seen, with the root-mean-square error between the model and the experimental data for both the voltage and temperature are well under 1%. This indicates that both models' ability to predict the battery response to inputs that it was not calibrated for: The battery cell electrical and thermal submodels are thus validated by experimental data.

A.4. Aging model calibration error metrics

This section contains a detailed breakdown of the root-mean-square error metrics between the calibrated model and the experimental data points. Here, three different levels of averaging are considered. First, the RMSE that is averaged over all of the accumulation variables is considered, Ah-throughput for cycling-based aging and storage time for calendar aging. For example, in cycling-based aging, this error metric would be computed as:

$$\text{RMSE}^{(1)}_{\ell,k} = \sqrt{\frac{1}{N_{\text{Ah}}}\sum_{j=1}^{N_{\text{Ah}}}\left[Q^{\text{model}}_{\text{loss}}(\text{Ah}_j,(T_{\text{cell}})_\ell,(I_C)_k;\theta^*,\zeta^*) - Q^{\text{data}}_{\text{loss}}(\text{Ah}_j;(T_{\text{cell}})_\ell,(I_C)_k)\right]^2} \tag{A.2}$$

Also reported is the RMSE associated at a fixed temperature, as this variable is common to both cycling and calendar-based aging:

$$\text{RMSE}^{(2)}_{\ell} = \sqrt{\frac{1}{N_{I_C}}\sum_{k=1}^{N_{I_C}}\frac{1}{N_{\text{Ah}}}\sum_{j=1}^{N_{\text{Ah}}}\left[Q^{\text{model}}_{\text{loss}}(\text{Ah}_j,(T_{\text{cell}})_\ell,(I_C)_k;\theta^*,\zeta^*) - Q^{\text{data}}_{\text{loss}}(\text{Ah}_j;(T_{\text{cell}})_\ell,(I_C)_k)\right]^2} \tag{A.3}$$

Finally, the total RMSE is reported which is computed over the full dataset across all conditions (see Box I). For cycling aging these error metrics are reported in Table A.6, while the calendar aging error metrics are reported in Table A.7.

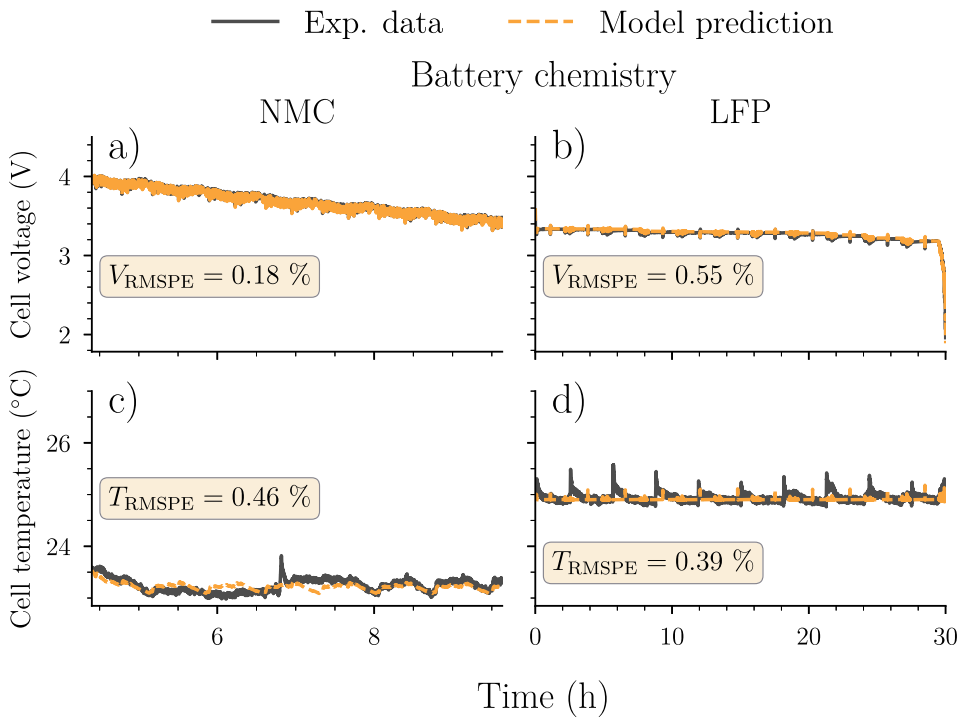

Fig. A.22. Validation of the battery cell electrical and thermal model predictions for NMC (a and c) and LFP (b and d) battery chemistries using experimental data. Solid black line: experimentally collected data. Dashed orange line: calibrated model predictions.

$$\text{RMSE}^{(3)} = \sqrt{\frac{1}{N_{T_{\text{cell}}}} \sum_{\ell=1}^{N_{T_{\text{cell}}}} \frac{1}{N_{I_C}} \sum_{k=1}^{N_{I_C}} \frac{1}{N_{\text{Ah}}} \sum_{j=1}^{N_{\text{Ah}}} \left[Q_{\text{loss}}^{\text{model}}(\text{Ah}_j, (T_{\text{cell}})_\ell, (I_C)_k; \theta^*, \zeta^*) - Q_{\text{loss}}^{\text{data}}(\text{Ah}_j; (T_{\text{cell}})_\ell, (I_C)_k) \right]^2} \tag{A.4}$$

Box I.

Table A.6
Calibration error metrics for the cycling aging submodels for the battery cell chemistries considered.

Chemistry	C-rate (1/h)	Temp. (°C)	RMSE (%)	Avg. RMSE at fixed temp. (%)	Tot. RMSE (%)
NMC	1	15	1.805	1.805	2.193
	1/2	25	0.964	2.398	
	1	25	2.467		
	2	25	4.257		
	3	25	1.905		
	1	35	1.287	1.287	
LFP	1	15	0.281	0.281	1.170
	1/2	25	2.102	1.264	
	1	25	0.446		
	2	25	2.629		
	3	25	2.459		
	1	35	1.170	1.176	

Table A.7
Calibration error metrics for the calendar aging submodels for the battery cell chemistries considered.

Chemistry	SoC (%)	Temp. (°C)	RMSE (%)	Avg. RMSE at fixed temp (%)	Tot. RMSE (%)
NMC	0	25	0.374	0.446	0.937
	25	25	0.176		
	50	25	0.636		
	75	25	0.548		
	100	25	0.342		
	0	50	0.339	1.248	
	25	50	0.900		
	50	50	1.098		
	75	50	0.999		
	100	50	2.159		
LFP	50	24	0.881	1.042	1.595
	100	24	1.202		
	50	45	1.167	1.631	
	100	45	2.095		
	50	60	1.252	1.340	
	100	60	1.429		
	50	85	3.370	2.368	
	100	85	1.366		

Data availability

Data will be made available on request.

References

[1] Cunanan C, Tran M-K, Lee Y, Kwok S, Leung V, Fowler M. A review of heavy-duty vehicle powertrain technologies: diesel engine vehicles, battery electric vehicles, and hydrogen fuel cell electric vehicles. Clean Technol 2021;3(2):474–89. http://dx.doi.org/10.3390/cleantechnol3020028.

[2] Huertas JI, Mogro AE, Jiménez JP. Configuration of electric vehicles for specific applications from a holistic perspective. WEVJ 2022;13(2):29. http://dx.doi.org/10.3390/wevj13020029.

[3] Fleming KL, Brown AL, Fulton L, Miller M. Electrification of medium- and heavy-duty ground transportation: status report. Curr Sustain Renew Energy Rep 2021;8(3):180–8. http://dx.doi.org/10.1007/s40518-021-00187-3.

[4] Forrest K, M. Mac Kinnon B Tarroja, Samuelsen S. Estimating the technical feasibility of fuel cell and battery electric vehicles for the medium and heavy duty sectors in California. Appl Energy 2020;276:115439. http://dx.doi.org/10.1016/j.apenergy.2020.115439.

[5] Nykvist B, Olsson O. The feasibility of heavy battery electric trucks. Joule 2021;5(4):901–13. http://dx.doi.org/10.1016/j.joule.2021.03.007.

[6] Catenaro E, Rizzo DM, Onori S. Experimental analysis and analytical modeling of enhanced-ragone plot. Appl Energy 2021;291:116473. http://dx.doi.org/10.1016/j.apenergy.2021.116473.

[7] Keil P, Schuster SF, Wilhelm J, Travi J, Hauser A, Karl RC, Jossen A. Calendar aging of lithium-ion batteries: I, impact of the graphite anode on capacity fade. J Electrochem Soc 2016;163(9):A1872–80. http://dx.doi.org/10.1149/2.0411609jes.

[8] Armand M, Axmann P, Bresser D, Copley M, Edström K, Ekberg C, Guyomard D, Lestriez B, Novák P, Petranikova M, Porcher W, Trabesinger S, Wohlfahrt-Mehrens M, Zhang H. Lithium-ion batteries – current state of the art and anticipated developments. J Power Sources 2020;479:228708. http://dx.doi.org/10.1016/j.jpowsour.2020.228708.

[9] Han X, Lu L, Zheng Y, Feng X, Li Z, Li J, Ouyang M. A review on the key issues of the lithium ion battery degradation among the whole life cycle. ETransportation 2019;1. http://dx.doi.org/10.1016/j.etran.2019.100005.

[10] Barcellona S, Piegari L. Effect of current on cycle aging of lithium ion batteries. J Energy Storage 2020;29:101310. http://dx.doi.org/10.1016/j.est.2020.101310.

[11] Dubarry M, Qin N, Brooker P. Calendar aging of commercial li-ion cells of different chemistries – a review. Curr Opin Electrochem 2018;9:106–13. http://dx.doi.org/10.1016/j.coelec.2018.05.023.

[12] Suri G, Onori S. A control-oriented cycle-life model for hybrid electric vehicle lithium-ion batteries. Energy 2016;96:644–53. http://dx.doi.org/10.1016/j.energy.2015.11.075.

[13] Naumann M, Schimpe M, Keil P, Hesse HC, Jossen A. Analysis and modeling of calendar aging of a commercial LiFePO4/graphite cell. J Energy Storage 2018;17:153–69. http://dx.doi.org/10.1016/j.est.2018.01.019.

[14] Nájera J, Arribas J, Castro R De, Núñez C. Semi-empirical ageing model for LFP and NMC Li-ion battery chemistries. J Energy Storage 2023;72:108016. http://dx.doi.org/10.1016/j.est.2023.108016.

[15] Vermeer W, Mouli GR Chandra, Bauer P. A comprehensive review on the characteristics and modeling of lithium-ion battery aging. IEEE Trans Transp Electrific. 2022;8(2):2205–32. http://dx.doi.org/10.1109/TTE.2021.3138357.

[16] Jafari M, Gauchia A, Zhao S, Zhang K, Gauchia L. Electric vehicle battery cycle aging evaluation in real-world daily driving and vehicle-to-grid services. IEEE Trans Transp Electrific. 2018;4(1):122–34. http://dx.doi.org/10.1109/TTE.2017.2764320.

[17] Yang Z, Patil D, Fahimi B. Electrothermal modeling of lithium-ion batteries for electric vehicles. IEEE Trans Veh Technol 2019;68(1):170–9. http://dx.doi.org/10.1109/TVT.2018.2880138.

[18] Tanim TR, Shirk MG, Bewley RL, Dufek EJ, Liaw BY. Fast charge implications: pack and cell analysis and comparison. J Power Sources 2018;381:56–65. http://dx.doi.org/10.1016/j.jpowsour.2018.01.091.

[19] S S, Manjarekar NS, Barik S. Soc estimation and IoT based delayed charging of electric vehicles. In: 2022 second international conference on power, Control and Computing Technologies (ICPC2T). Raipur, India: IEEE; 2022, p. 1–6. http://dx.doi.org/10.1109/ICPC2T53885.2022.9776936.

[20] Tomaszewska A, Chu Z, Feng X, S. O'Kane X Liu, Chen J, Ji C, Endler E, Li R, Liu L, Li Y, Zheng S, Vetterlein S, Gao M, Du J, Parkes M, Ouyang M, Marinescu M, Offer G, Wu B. Lithium-ion battery fast charging: A review. eTransportation 2019;1:100011. http://dx.doi.org/10.1016/j.etran.2019.100011.

[21] Pelletier S, Jabali O, Laporte G. Charge scheduling for electric freight vehicles. Transp Res Part B: Methodol 2018;115:246–69. http://dx.doi.org/10.1016/j.trb.2018.07.010.

[22] Yang F, Xie Y, Deng Y, Yuan C. Predictive modeling of battery degradation and greenhouse gas emissions from U.S. state-level electric vehicle operation. Nat Commun 2018;9(1):2429. http://dx.doi.org/10.1038/s41467-018-04826-0.

[23] Ceraolo M, Fioriti D, Lutzemberger G, Quilici F Giuseppe, Scarpelli C, Bianchi F. Electro-thermal modeling and aging evaluation of lithium battery packs for electric vehicles. IEEE Access 2024;12:128151–65. http://dx.doi.org/10.1109/ACCESS.2024.3430104.

[24] Karunarathna JS, Madawala UK, Sandelic M, Blaabjerg F, Baguley C. The impact of operational and environmental conditions on battery lifetime in fast electric vehicle charging systems. IEEE Trans Power Electron 2024;39(4):4645–56. http://dx.doi.org/10.1109/TPEL.2023.3342121.

[25] Onori S, Serrao L, Rizzoni G. Hybrid electric vehicles: energy management strategies. Springer Publishing Company; 2016, http://dx.doi.org/10.1007/978-1-4471-6781-5.

[26] Hyttinen J, Ussner M, R. Österlöf J Jerrelind, Drugge L. Truck tyre transient rolling resistance and temperature at varying vehicle velocities - measurements and simulations. Polymer Testing 2023;122(5). http://dx.doi.org/10.1016/J.POLYMERTESTING.2023.108004.

[27] Nigel. Battery pack mass estimation. 2022, https://www.batterydesign.net/battery-pack-mass-estimation/.

[28] T680e | kenworth. https://www.kenworth.com/trucks/t680e/.

[29] Gao Z, Finney C, Daw C, LaClair TJ, Smith D. Comparative study of hybrid powertrains on fuel saving, emissions, and component energy loss in hd trucks. SAE Int J Commer Veh 2014;7:414–31. http://dx.doi.org/10.4271/2014-01-2326, https://www.sae.org/publications/technical-papers/content/2014-01-2326/.

[30] Shiledar A, Villani M, Lucero JNE, Sun R, Sujan VA, Onori S, Rizzoni G. Assessing geographical and seasonal influences on energy efficiency of electric drayage trucks. 2025, http://dx.doi.org/10.48550/arXiv.2504.02575, eess. http://arxiv.org/abs/2504.02575.

[31] Dettù F, Pozzato G, Rizzo DM, Onori S. Exergy-based modeling framework for hybrid and electric ground vehicles. Appl Energy 2021;300:117320. http://dx.doi.org/10.1016/j.apenergy.2021.117320.

[32] Rahn CD, Wang CY. Battery systems engineering. Wiley; 2013.

[33] Van der Ven A, See KA, Pilon L. Hysteresis in electrochemical systems. Batter Energy 2022;1(2):20210017. http://dx.doi.org/10.1002/bte2.20210017.

[34] Plett GL. Extended Kalman filtering for battery management systems of LiPB-based HEV battery packs. J Power Sources 2004;134(2):262–76. http://dx.doi.org/10.1016/j.jpowsour.2004.02.032.

[35] Plett G. Battery management systems, volume I: battery modeling. Artech House power engineering series, Artech House; 2015.

[36] Gao Lijun, Liu Shengyi, Dougal R. Dynamic lithium-ion battery model for system simulation. IEEE Trans Comp Packag Technol 2002;25(3):495–505. http://dx.doi.org/10.1109/TCAPT.2002.803653.

[37] Lin X, Perez HE, Mohan S, Siegel JB, Stefanopoulou AG, Ding Y, Castanier MP. A lumped-parameter electro-thermal model for cylindrical batteries. J Power Sources 2014;257:1–11. http://dx.doi.org/10.1016/j.jpowsour.2014.01.097.

[38] Teichert O, Schneider J, Lienkamp M. Strategy beats power: Cooling system design for battery-electric long-haul trucks. 2022.

[39] Baghdadi I, Briat O, Delétage J-Y, Gyan P, Vinassa J-M. Lithium battery aging model based on dakin's degradation approach. J Power Sources 2016;325:273–85. http://dx.doi.org/10.1016/j.jpowsour.2016.06.036.

[40] E. Redondo-Iglesias P Venet, Pelissier S. Modelling lithium-ion battery ageing in electric vehicle applications—calendar and cycling ageing combination effects. Batteries 2020;6(1):14. http://dx.doi.org/10.3390/batteries6010014.

[41] Serrao L, Onori S, Rizzoni G, Guezennec Y. A novel model-based algorithm for battery prognosis. IFAC Proc Vol 2009;42(8):923–8. http://dx.doi.org/10.3182/20090630-4-ES-2003.00152.

[42] Lucero JN E, Sujan VA, Onori S. An experimentally validated electro-thermal EV battery pack model incorporating cycle-life aging and cell-to-cell variations. IEEE Trans. Transp. Electrific. 2024. http://dx.doi.org/10.1109/TTE.2024.3365028, 1–1.

[43] Piombo G, Fasolato S, Heymer R, Hidalgo M, Niri M Faraji, Onori S, Marco J. Unveiling the performance impact of module level features on parallel-connected lithium-ion cells via explainable machine learning techniques on a full factorial design of experiments. J Energy Storage 2024;84:110783. http://dx.doi.org/10.1016/j.est.2024.110783.

[44] Campestrini C, Keil P, Schuster SF, Jossen A. Ageing of lithium-ion battery modules with dissipative balancing compared with single-cell ageing. J Energy Storage 2016;6:142–52. http://dx.doi.org/10.1016/j.est.2016.03.004.

[45] Petit M, Prada E, Sauvant-Moynot V. Development of an empirical aging model for li-ion batteries and application to assess the impact of vehicle-to-grid strategies on battery lifetime. Appl Energy 2016;172:398–407. http://dx.doi.org/10.1016/j.apenergy.2016.03.119.

[46] Apostolaki-Iosifidou E, Codani P, Kempton W. Measurement of power loss during electric vehicle charging and discharging. Energy 2017;127:730–42. http://dx.doi.org/10.1016/j.energy.2017.03.015, https://www.sciencedirect.com/science/article/pii/S0360544217303730.

[47] USEnvironmental Protection Agency. Energy star electric vehicle chargers. 2025, https://www.energystar.gov/products/ev_chargers. [Accessed 27 March 2025].

[48] Wanbang Digital Energy Co, Ltd. Energy star certified ev charger: star charge dc2400an06702. 2025, https://www.energystar.gov/productfinder/product/certified-evse/details/2508238, eNERGY STAR Unique ID: 2508238. Certified on 2023-05-31. Document captured on 2025-03-27.

[49] Daina N, Sivakumar A, Polak JW. Modelling electric vehicles use: a survey on the methods. Renew Sustain Energy Rev 2017;68:447–60. http://dx.doi.org/10.1016/J.RSER.2016.10.005.

[50] Shiri S, Huynh N. Assessment of u. s chassis supply models on drayage productivity and air emissions. Transp Res Part D: Transp Environ 2018;61:174–203. http://dx.doi.org/10.1016/J.TRD.2017.04.024.

[51] Sujan V, Fan J, Jatana G, Sun R. Nationally scalable hydrogen fueling infrastructure deployment: A megaregion analysis and optimization approach. 2024, arXiv preprint.

[52] TRBoard, of Sciences Engineering, Medicine. Truck drayage productivity guide. The National Academies Press; 2011, http://dx.doi.org/10.17226/14536, https://nap.nationalacademies.org/catalog/14536/truck-drayage-productivity-guide.

[53] Summary of hours of service regulations | fmcsa. https://www.fmcsa.dot.gov/regulations/hours-service/summary-hours-service-regulations.

[54] Preger Y, Barkholtz HM, Fresquez A, Campbell DL, Juba BW, Romàn-Kustas J, Ferreira SR, Chalamala B. Degradation of commercial lithium-ion cells as a function of chemistry and cycling conditions. J Electrochem Soc 2020;167(12):120532. http://dx.doi.org/10.1149/1945-7111/abae37.

[55] Jaguemont J, Boulon L, Dubé Y. A comprehensive review of lithium-ion batteries used in hybrid and electric vehicles at cold temperatures. Appl Energy 2016;164:99–114. http://dx.doi.org/10.1016/j.apenergy.2015.11.034.

[56] Shen W, Wang N, Zhang J, Wang F, Zhang G. Heat generation and degradation mechanism of lithium-ion batteries during high-temperature aging. ACS Omega 2022;7(49):44733–42. http://dx.doi.org/10.1021/acsomega.2c04093.

[57] Hamar JC, Stuckenberger M, Sturm J, Schmitt J, Rogge M, Erhard SV, Jossen A. Investigating the path dependent aging behavior of nickel cobalt aluminum oxide cathode batteries during high C-rate cycling conditions. J Electrochem Soc 2024;171(2):020555. http://dx.doi.org/10.1149/1945-7111/ad2952.

[58] Teichert O, Link S, Schneider J, Wolff S, Lienkamp M. Techno-economic cell selection for battery-electric long-haul trucks. ETransportation 2023;16. http://dx.doi.org/10.1016/j.etran.2022.100225.

[59] Lam VN, Cui X, Stroebl F, Uppaluri M, Onori S, Chueh WC. A decade of insights: delving into calendar aging trends and implications. Joule 2024. http://dx.doi.org/10.1016/j.joule.2024.11.013, S2542435124005105.

[60] Mihelic R, Roeth M. Electric trucks—where they make sense. Guidance report, Fort Wayne: North American Council for Freight Efficiency (NACFE; 2018, https://nacfe.org/research/emerging-technologies/electric-trucks/electric-trucks-where-they-make-sense/.

[61] Kane M. Tesla model s plaid fast charging analysis. 2021, https://insideevs.com/news/{515641}/tesla-models-plaid-charging-analysis/. [Accessed 27 March 2025].

[62] Sujan VA, Siekmann A, Tennille S, Tsybina E. Designing dynamic wireless power transfer corridors for heavy duty battery electric commercial freight vehicles. In: WCX sAE world congress experience. Detroit, Michigan, United States; 2023, p. 2023–01–0703. http://dx.doi.org/10.4271/2023-01-0703.

[63] Wu H. A survey of battery swapping stations for electric vehicles: operation modes and decision scenarios. IEEE Trans Intell Transp Syst 2022;23(8):10163–85. http://dx.doi.org/10.1109/TITS.2021.3125861.

[64] Zhu F, Li L, Li Y, Li K, Lu L, Han X, Du J, Ouyang M. Does the battery swapping energy supply mode have better economic potential for electric heavy-duty trucks?. ETransportation 2023;15. http://dx.doi.org/10.1016/j.etran.2022.100215.

[65] Shi P, Ni G, Jin R, Wang H, Wang J, Sun Z, Qiu G. Multi-timescale battery-charging optimization for electric heavy-duty truck battery-swapping stations, considering source–load–storage uncertainty. Energies 2025;18(2):241. http://dx.doi.org/10.3390/en18020241.

[66] Wang Z, Hou S, Guo W. Inventory management of battery swapping and charging stations considering uncertainty. Int J Electr Power Energy Syst 2024;155:109528. http://dx.doi.org/10.1016/j.ijepes.2023.109528.

[67] Sujan VA, Sun R, Snyder I. Or-agent framework – architecting electrified heavy-duty drayage applications. Appl Energy 2025;386:125540. http://dx.doi.org/10.1016/j.apenergy.2025.125540, https://www.sciencedirect.com/science/article/pii/S0306261925002703.

[68] Electric Trucks Have Arrived. The use case for heavy-duty regional haul tractors. Tech. rep., North American Council for Freight Efficiency (NACFE; 2022, https://nacfe.org/research/run-on-less/run-on-less-electric/hd-regional-haul-tractors/#top.

[69] NACFE: Run on Less – Electric DEPOT. http://nacfe.org/research/run-on-less/run-on-less-electric-depot/.

[70] Zhou X, Han X, Wang Y, Lu L, Ouyang M. A data-driven lifepo4 battery capacity estimation method based on cloud charging data from electric vehicles. Batteries 2023;9(3). http://dx.doi.org/10.3390/batteries9030181, company: Multidisciplinary Digital Publishing Institute Distributor: Multidisciplinary Digital Publishing Institute Institution: Multidisciplinary Digital Publishing Institute Label: Multidisciplinary Digital Publishing Institute publisher. https://www.mdpi.com/2313-0105/9/3/181.

[71] Zhou X, Han X, Shi K, Chen X, Guo D, Zheng Y, Lu L, Ouyang M. Intelligent battery life management through mechanism and machine learning under real vehicle working conditions. J Power Sources 2025;640:236749. http://dx.doi.org/10.1016/j.jpowsour.2025.236749, https://www.sciencedirect.com/science/article/pii/S0378775325005853.

[72] Fioriti D, Scarpelli C, Pellegrino L, Lutzemberger G, Micolano E, Salamone S. Battery lifetime of electric vehicles by novel rainflow-counting algorithm with temperature and c-rate dynamics: Effects of fast charging, user habits, vehicle-to-grid and climate zones. J Energy Storage 2023;59:106458. http://dx.doi.org/10.1016/j.est.2022.106458, https://www.sciencedirect.com/science/article/pii/S2352152X22024471.

[73] Geslin A, Xu L, Ganapathi D, Moy K, Chueh WC, Onori S. Dynamic cycling enhances battery lifetime. Nat Energy 2024. http://dx.doi.org/10.1038/s41560-024-01675-8.

[74] Park S, Lee H, Choi S, Lim J, Kim S, Song J, Ali M, Kwon T-S, Doh C, Lee YM. Microstructure-based digital twin thermo-electrochemical modeling of LIBs at the cell-to-module scale. eTransportation 2024;22:100370. http://dx.doi.org/10.1016/j.etran.2024.100370, https://www.sciencedirect.com/science/article/pii/S2590116824000602.

[75] Díaz-Ramirez J, Giraldo-Peralta N, Flórez-Ceron D, Rangel V, Mejía-Argueta C, Huertas JI, Bernal M. Eco-driving key factors that influence fuel consumption in heavy-truck fleets: A colombian case. Transp Res Part D: Transp Environ 2017;56:258–70. http://dx.doi.org/10.1016/j.trd.2017.08.012, https://www.sciencedirect.com/science/article/pii/S1361920916308689.

[76] Younes S, Oloufa A. Applying topological information for routing commercial vehicles around traffic congestion. Appl Sci 2024;14(22). http://dx.doi.org/10.3390/app142210134, https://www.mdpi.com/2076-3417/14/22/10134.

[77] Ahmed R, Gazzarri J, Onori S, Habibi S, Jackey R, Rzemien K, Tjong J, LeSage J. Model-based parameter identification of healthy and aged li-ion batteries for electric vehicle applications. SAE Int J Alt Power. 2015;4(2):233–47. http://dx.doi.org/10.4271/2015-01-0252.

[78] Pozzato G, Allam A, Onori S. Lithium-ion battery aging dataset based on electric vehicle real-driving profiles. Data Brief 2022;41:107995. http://dx.doi.org/10.1016/j.dib.2022.107995.

[79] Gao Y, Nguyen T, Onori S. Model-based state-of-charge estimation of 28 V $LiFePO_4$ aircraft battery. SAE Int J Elec. Veh 2024;14(1):14–14–01–0003. http://dx.doi.org/10.4271/14-14-01-0003.

[80] M. Kochenderfer T Wheeler. Algorithms for optimization. MIT Press; 2019.

[81] Chem L. Lithium ion inr21700 m50 battery cell datasheet. 2016, Product specification document, Rev 0, confidential..

[82] LWInc. 26650 lithium ion power cell datasheet. In: Product specification document, rev 3, January 2023. nanophosphate® Technology; 2023, https://www.lithiumwerks.com/contact.

[83] Agency United States Environmental Protection. EPA urban dynamometer driving schedule (UDDS). 2024, https://www.epa.gov/emission-standards-reference-guide/epa-urban-dynamometer-driving-schedule-udds. [Accessed 09 December 2024].